Scaling the vorticity dynamics in the leading-edge vortices of revolving wings with two directional length scales

Cite as: Phys. Fluids **32**, 121903 (2020); https://doi.org/10.1063/5.0024213 Submitted: 05 August 2020 . Accepted: 18 November 2020 . Published Online: 22 December 2020

📵 Nathaniel H. Werner, 📵 Junshi Wang, 📵 Haibo Dong, 📵 Azar Eslam Panah, and 📵 Bo Cheng







ARTICLES YOU MAY BE INTERESTED IN

Effects of time-varying flexibility on the propulsion performance of a flapping foil Physics of Fluids 32, 121904 (2020); https://doi.org/10.1063/5.0027927

Computational analysis of hydrodynamic interactions in a high-density fish school Physics of Fluids **32**, 121901 (2020); https://doi.org/10.1063/5.0028682

Tip vortices formation and evolution of rotating wings at low Reynolds numbers Physics of Fluids 32, 021905 (2020); https://doi.org/10.1063/1.5134689

Physics of Fluids
SPECIAL TOPIC: Tribute to
Frank M. White on his 88th Anniversary





Scaling the vorticity dynamics in the leading-edge vortices of revolving wings with two directional length scales

Cite as: Phys. Fluids 32, 121903 (2020); doi: 10.1063/5.0024213 Submitted: 5 August 2020 • Accepted: 18 November 2020 •









Published Online: 22 December 2020





Nathaniel H. Werner, 1 D Junshi Wang, 2 D Haibo Dong, 2 D Azar Eslam Panah, 3 D and Bo Cheng 1.0 D





AFFILIATIONS

- Department of Mechanical Engineering, Pennsylvania State University, University Park, Pennsylvania 16802, USA
- ²Department of Mechanical and Aerospace Engineering, University of Virginia, Charlottesville, Virginia 22904, USA
- Department of Mechanical Engineering, Pennsylvania State University, Berks, Reading, Pennsylvania 19610, USA

ABSTRACT

In revolving or flapping wings, radial planetary vorticity tilting (PVTr) is a mechanism that contributes to the removal of radial (spanwise) vorticity within the leading-edge vortex (LEV), while vorticity advection increases its strength. Dimensional analysis predicts that the PVTr and advection should scale with the wing aspect-ratio (AR) in identical fashion, assuming a uniform characteristic length is used. However, the authors' previous work suggests that the vorticity advection decreases more rapidly than the PVTr as AR increases, indicating that separate normalizations should be applied. Here, we aim to develop a comprehensive scaling for the PVTr and vorticity advection based on simulation results using computational fluid dynamics. Two sets of simulations of revolving rectangular wings at an angle of attack of 45° were performed, the first set with the wing-tip velocity maintained constant, so that the Reynolds number (Re) defined at the radius of gyration equals 110, and the second set with the wing angular velocity maintained constant, so that Re defined at one chord length equals 63.5. We proposed two independent length scales based on LEV geometry, i.e., wing-span for the radial and tangential directions and wing chord for the vertical direction. The LEV size in the radial and tangential directions was limited by the wing-span, while the vertical depth remained invariant. The use of two length scales successfully predicted not only the scaling for the PVTr and the vorticity advection but also the relative magnitude of advection in three directions, i.e., tangential advection was strongest, followed by the vertical (downwash) and then the radial that was negligible.

Published under license by AIP Publishing. https://doi.org/10.1063/5.0024213

I. INTRODUCTION

Insect wings generate highly three-dimensional flow structures; of particular interest are the stably attached leading-edge vortices (LEVs), 1-3 which are also observed over the wings of small birds and bats, 5 as well as steadily revolving wings with high angle of attack (AoA). 3,6-9 LEVs manifest in flows with revolving wings at Reynolds numbers (Re) on the order of $O(10^2)$ – $O(10^4)^{10,11}$ and poststall angles of attack $AoA \ge 45^{\circ}$, 12 with a relatively low wing aspectratio $(AR)^{8,13}$ in comparison with those in helicopter propellers. The wing's aspect-ratio, AR = s/c (using the half-span definition 15), is arguably the most important parameter among all of the dimensionless numbers characterizing insect and revolving wings as it governs

the three-dimensional vortex topology and the underlying vorticity dynamics. AR is also proportional to the Rossby number (Ro) in general, 8,9 which is defined as the ratio of advective and Coriolis accelerations.1

Numerous studies have investigated the scaling of the vorticity dynamics present in a stable LEV with AR. Lentink and Dickinson⁸ showed that for the insects in hover, and by analogy revolving wings, the Coriolis and centripetal accelerations (i.e., rotational mechanisms) scale inversely with AR. Therefore, since the wing *AR*s of fliers in nature are only of order one (typically less than 3), these rotational mechanisms at smaller ARs promote the attachment and stability of the LEV. Several subsequent studies focusing on these rotational mechanisms further suggested that the Coriolis

a) Author to whom correspondence should be addressed: buclo@psu.edu

acceleration, not the centripetal, plays a major role in LEV attachment and stability. ^{18–22} In Lentink's study, and several since then, it was implicitly assumed that the wing chord was an appropriate length scale for normalizing the Navier–Stokes equations likely due to this being the common length scale used in the literature. ²³

Other studies have investigated advective mechanisms related to the transport of vorticity due to the combined effect of local flow and spatial gradients in vorticity. 16 For example, the radial advection due to the spanwise flow (induced by the spanwise pressure gradient²⁴) and vertical advection (downwash) behind the wing²⁵ drain vorticity from the LEV region after being transported from the leading-edge into the LEV by the tangential advection. 27 Several experimental studies^{27,28} and others using simulations^{29–31} of revolving wings at similar AR and Re to those in nature observed negligible radial advection. Another study by Han, Chang, and Cho³² using experimentally revolving wings also observed that the downwash was weaker at higher ARs. Others noted that the vertical advection induced by the tip vortex (TiV) also promotes LEV attachment. However, the effect is limited to only the most distal regions of the wing; Jardin, Farcy, and David³³ and DeVoria and Mohseni³⁴ pointed out the size of TiV extends only up to 1.4-1.5 chord lengths from the tip, therefore, the vertical advection is only effective in maintaining LEV attachment for small AR wings below the average value found in nature.^{8,13} These results suggest that the LEV can be divided into at least two regions: the main LEV and a separate more three-dimensional tip region. Since the TiV is a highly three-dimensional region within the LEV, the flow profiles in this region will differ from those in the main portion of the LEV. In other words, these flow profiles are considered to be geometrically dissimilar to those found in the majority of the LEV. Geometrically similar flow profiles are here defined as those that fall within one standard deviation above or below the mean profile taken across the whole wing-span within the LEV. Using this definition, the regions where the flow profiles differ significantly from the mean will be removed and not considered in the primary analysis.

In previous work, Werner et al. 35 demonstrated that the effect of Coriolis acceleration on the vorticity dynamics removes radial LEV vorticity by tilting planetary vorticity in the opposite direction via the vertical gradient of spanwise velocity. They called this mechanism the radial planetary vorticity tilting (PVTr). A set of scaling terms was developed based on the characteristic magnitudes used by Lentink and Dickinson⁸ and Cheng et al.²⁷ and applied to normalize the PVTr and vorticity advection in order to understand their global scaling behavior with AR and Re. Based on the original analysis of Werner et al., it was predicted that both the PVTr and vorticity advection would scale with AR similarly at constant Re if the same length scale was used; however, this was shown to not be true. The normalized PVTr was roughly constant with increasing AR, while the vorticity advection was observed to decrease with increasing AR. This led the authors to conclude that separate length scales should be used for the PVTr and vorticity advection terms, and this needed further investigation.

In the study by Lentink and Dickinson⁸ and many in the literature, the wing chord was used as the single characteristic length scale for normalizing the Navier–Stokes equations, which is traditionally the length scale for translating wings.²³ Harbig, Sheridan, and Thompson³⁶ proposed the wing-span, instead of the chord, for use as the characteristic length scale due to the intense radial

velocity in the core of the main LEV as observed by Dickinson, Lehmann, and Sane⁶ and Birch, Dickson, and Dickinson,⁷ which enables the LEV to grow in size and in strength along the wing-span. Specifically, they defined a span-based Reynolds number (Re_s) and showed that holding it constant better accounted for the changes in the flow structure of the LEV as AR varies (via changing the wing chord while maintaining a constant span). Using the span as the single length scale results in a normalized vorticity advection that is roughly constant with AR, while the PVTr increases linearly indicating that the span is better suited for the vorticity advection but not for the PVTr.

While one of the implicit assumptions made throughout the literature was that only one length scale was necessary for correctly scaling the vorticity dynamics of revolving wings with an attached LEV, we demonstrate, in this work, that at least two length scales are required, i.e., the length scales are anisotropic. Since the wings are finite, and the flow field is inherently three-dimensional, this can be expected since the flows resemble those in propellers and turbine blades near the root. 37,38 In this study, we provide further evidence and analyses for the proposed anisotropic scaling. We also discuss other complexities that need to be considered when applying the proposed scaling terms, such as non-linear effects in the local trends and additional *Re* dependence.

II. METHODS

A. Numerical methods

In this work, revolving rectangular wings with three aspectratios AR = s/c = 3, 5, and 7 in the range of insects and humming-birds 8,13,39,40 were investigated (where s is the single wing-span and c is the chord). Each wing was rotated impulsively from rest at a constant angular velocity Ω for three full revolutions about a vertical axis aligned with the wing-root at the mid-chord (Fig. 1) until the flow reached a quasi-steady state. The wings all had a chord length of c=1 cm and an infinitesimal thickness, where the wing-span was changed for different ARs. Additionally, the angle of attack (AoA) of each wing was held constant at 45° for all three revolutions.

Two sets of simulations were performed: The first set used all three ARs with the wing velocity at the radius of gyration $U_g = \Omega r_g$ (or $U_{tip} = \Omega s$) maintained constant so that the Reynolds number defined at the radius of gyration (which simplifies to $s/\sqrt{3}$ for a rectangular wing 35,41 using Ellington's definition 39) was constant,

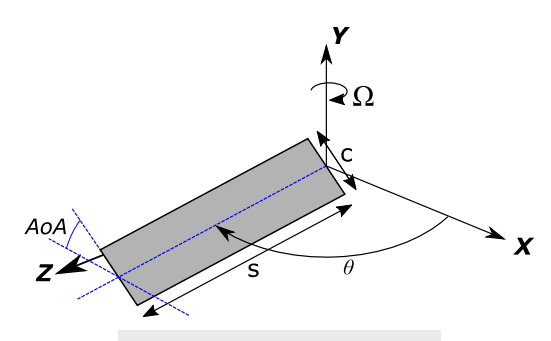


FIG. 1. Wing kinematics and geometry.

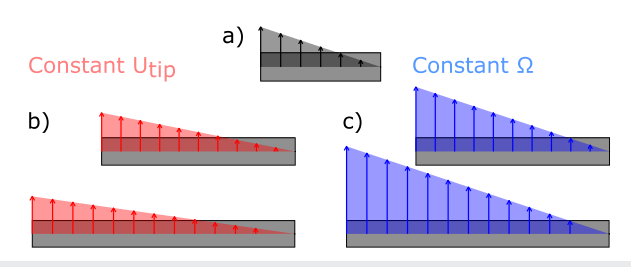


FIG. 2. (a) $Re_g = 110$, AR = 3. (b) Wings revolving at the constant wing-tip velocity: $Re_g = 110$, AR = 5 and 7. (c) Wings revolving at the constant angular velocity: $Re_c = 63.5$, AR = 5 ($Re_g = 183$) and 7 ($Re_g = 257$).

i.e., $Re_g = \Omega r_g c/v = 110$ [see Fig. 2(b)]. The second set used the same ARs but instead maintained a constant wing angular velocity Ω with the Reynolds number at one chord length from the root maintained constant, i.e., $Re_c = \Omega c^2/v = 63.5$ [see Fig. 2(c)]. These two Reynolds number definitions can be related to each other by $Re_g/Re_c = Ro$, where Ro is the Rossby number and is defined as the ratio of advective to Coriolis accelerations in the relative Navier–Stokes equation. ^{16,17} The value of Re_g was chosen to be comparable to that of fruit flies ($Drosophila\ melanogaster$), ^{6,36} while the value of Re_c was chosen so that the angular velocity was the same as that of the AR = 3 wing at $Re_g = 110$ [Fig. 2(a)]. The corresponding Re_g and tip Reynolds number $Re_{tip} = \Omega sc/v$ values at constant Re_c are given in Table I where it can be seen that they are all of the same order of magnitude. Finally, the density $\rho = 850 \text{ kg/m}^3$ and kinematic viscosity $v = 8 \times 10^{-6} \text{ m}^2/\text{s}$ were used in all simulations

A Cartesian computational grid with a stretching grid configuration was employed in the simulations, as shown in Fig. 3. A minimum grid spacing of 0.031c was used in the dense region for each of the three AR values, which was sufficient to resolve the nearfield vortex structures around the wing. A homogeneous Neumann boundary condition in pressure is applied to all six boundaries of the computational domain so that the vorticity could advect freely at the boundaries and a no-slip boundary condition was applied at the wing surfaces. The governing equations employed by the solver are the Navier–Stokes equations (excluding gravity) [Eq. (1a)] and the incompressibility condition [Eq. (1b)],

$$\dot{\mathbf{u}} = -(\mathbf{u} \cdot \nabla)\mathbf{u} - \frac{1}{\rho}\nabla p + \nu \nabla^2 \mathbf{u}, \tag{1a}$$

$$\nabla \cdot \mathbf{u} = 0. \tag{1b}$$

TABLE I. Aspect-ratios and Reynolds numbers used in simulations.

Re_c =	= 63.5
$\overline{\mathrm{Re}_{\mathrm{g}}}$	Re _{tip}
110	191
183	318
257	445
	Re _g 110 183

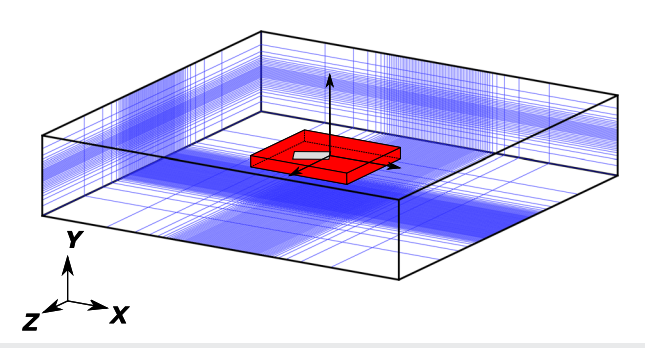


FIG. 3. Relative size of the grid chosen (blue) with the denser region (red) compared to the size of the wing. The rectangular domain has the size $50c \times 10c \times 50c$ with a dense mesh region in the center surrounded by the stretched meshes.

Here, \mathbf{u} is the velocity vector in the inertial reference frame, $\dot{\mathbf{u}}$ represents the time derivative of the velocity, p is the pressure, and ∇ nabla is the vector gradient. An in-house, finite-difference-based, Cartesian-grid, immersed-boundary-method solver was employed to solve the above equations. In this solver, the flow simulation with complex moving boundaries was achieved with stationary nonbody-conformal Cartesian grids to eliminate the need for a complex re-meshing algorithm, which was otherwise used by body-conformal methods. The solver can simulate flows of moving bodies with intricate geometry while still achieving second-order accuracy in both space and time. The equations were integrated in time using the fractional step method, and the boundary conditions on the immersed boundary were enforced by a ghost-cell procedure. This approach has been successfully applied to revolving wings,³ the flapping propulsion of insects, 45,46 birds, 47,48 fish, 49,50 ping plates,⁵¹ and human respiratory flows.⁵² A detailed description and validation of this solver can be found in the authors' previous work.4

A convergence test was performed using the lift coefficient data for four separate mesh sizes. Previously, it was shown by Werner *et al.*³⁵ for AR = 5 and $Re_g = 1400$ wings, that the lift had converged by the second half of the third revolution (at $\theta = 900^{\circ}$, or after three full revolutions), which corresponds to the time period where the flow was time averaged. Additionally, it was argued that the flow had reached a quasi-steady state by this time for $Re_g = 110$. For the sake of completeness, two similar convergence tests for AR = 5, $Re_g = 110$, and $Re_c = 63.5$ were performed due to the minor adjustments in the grid density from the previous study. Figures 4(a) and 4(b) show the local lift coefficients $C_L = F_L/\left(\frac{1}{2}\rho U_g^2 sc\right)$ with the increasing mesh size (where F_L is the dimensional lift force), and Figs. 4(c) and 4(d) show the time-averaged lift $\overline{C_L}$.

B. Vorticity dynamics

To describe the combined effect of advective and rotational mechanisms involved in the vorticity dynamics of LEVs, the Navier–Stokes equations [Eq. (1a)] are cast into a non-inertial rotating frame using the velocity of the rotating wing in order to identify the role of Coriolis and centripetal accelerations in the vorticity dynamics. The rotating frame is defined using the relative parameters (denoted with $^\prime$)

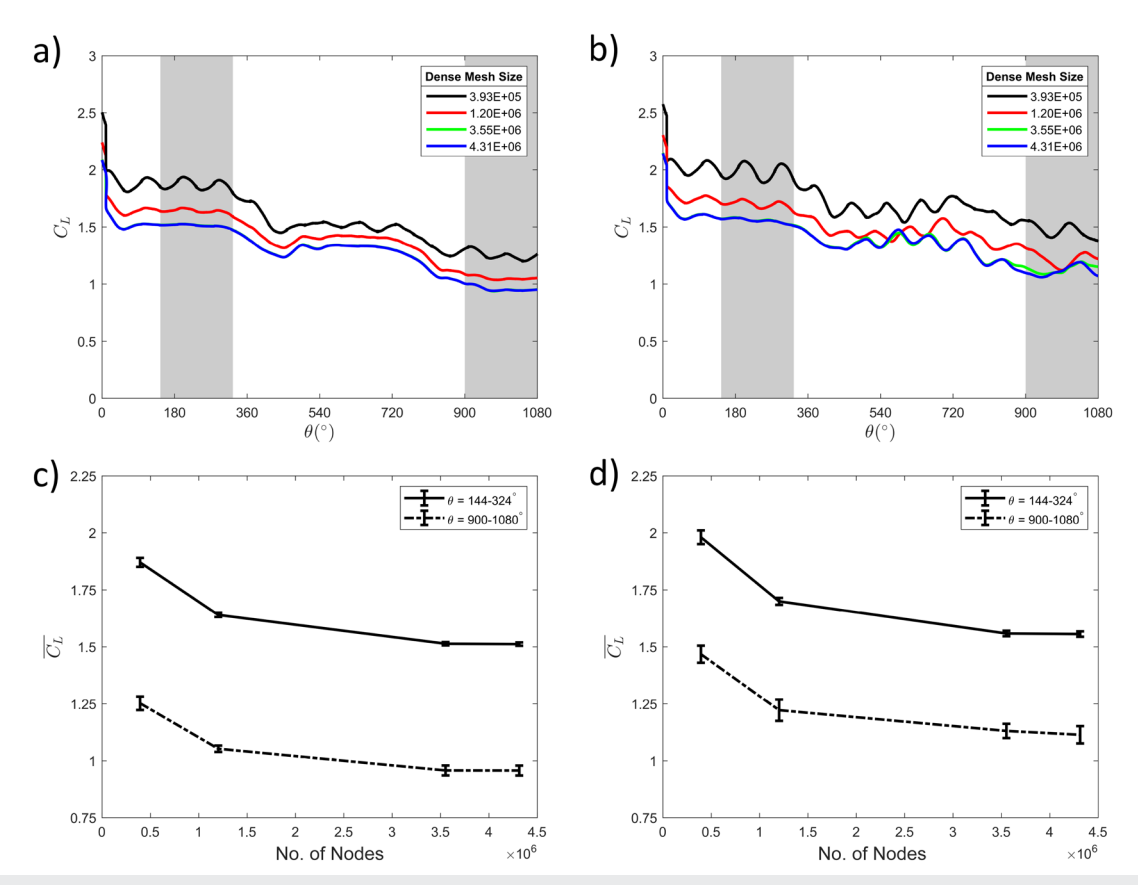


FIG. 4. Four mesh sizes are used with 3.93, 12, 35.5, and 43.1 \times 10⁵ nodes, respectively. The gray shaded regions correspond to the two time-averaging periods, θ = 144°-324° and 900°-1080°, respectively. $C_L = F_L/\left(\frac{1}{2}\rho U_g^2 sc\right)$ plotted against the revolution angle θ for (a) AR = 5, $Re_g = 110$ and (b) AR = 5, $Re_c = 63.5$. Time-averaged lift coefficient $\overline{C_L}$ for (c) AR = 5, $Re_g = 110$ and (d) AR = 5, $Re_c = 63.5$ plotted against numbers of nodes in each mesh with error bars representing one standard deviation of the lift coefficient from each time-averaging period. In (a), the blue curve almost overlaps with the green curve.

$$\mathbf{u}' = \mathbf{u} - \mathbf{\Omega} \times \mathbf{R},\tag{2a}$$

$$\nabla' = \nabla, \tag{2b}$$

$$p' = p. (2c)$$

The Navier–Stokes equation in the rotating frame [Eq. (3)] differs from that in the inertial frame by the addition of the Coriolis acceleration $-2\Omega \times \mathbf{u}'$ and centripetal acceleration $-\Omega \times (\Omega \times \mathbf{R})$,

$$\dot{\mathbf{u}}' = -\left(\mathbf{u}' \cdot \nabla\right)\mathbf{u}' - \frac{1}{\rho}\nabla p + \nu\nabla^2\mathbf{u}' - 2\mathbf{\Omega} \times \mathbf{u}' - \mathbf{\Omega} \times (\mathbf{\Omega} \times \mathbf{R}).$$
 (3)

A full derivation of Eq. (3) is provided by Kundu and Cohen. Additionally, others such as Lentink and Dickinson include an additional term for the angular acceleration (sometimes called the Euler acceleration in the the term drops out since our wings are revolving at a constant angular velocity. Next, the curl of relative Navier–Stokes equations is taken to obtain the vorticity equation in the rotating frame [Eq. (4)], where again a full derivation can be found in the study of Kundu and Cohen, if

$$\dot{\boldsymbol{\omega}}' = -(\mathbf{u}' \cdot \nabla)\boldsymbol{\omega}' + \nu \nabla^2 \boldsymbol{\omega}' + (2\boldsymbol{\Omega} \cdot \nabla)\mathbf{u}'. \tag{4}$$

From here onward, the ' is dropped from the equations, although all the quantities represent the flow variables (velocity and vorticity) in the rotating frame as if they were observed from the wing in motion.

For the purpose of data analysis, in addition to a fixed Cartesian frame (x, y, z), a rotated Cartesian frame (t, y, r) was defined based on the azimuthal angle ϕ of a fluid element (Fig. 5) identical to those used in the authors' previous work. ^{27,35} Vectors in the fixed Cartesian frame were transformed into those in the rotated Cartesian frame using the Jacobian matrix

$$J(\phi) = \begin{pmatrix} \sin \phi & 0 & -\cos \phi \\ 0 & 1 & 0 \\ \cos \phi & 0 & \sin \phi \end{pmatrix}. \tag{5}$$

Using Eq. (5), the radial component of Eq. (4) was derived and is given in Eq. (6a). The primary terms in the radial vorticity equation that are analyzed in this work are the vorticity advection $A = -(\mathbf{u} \cdot \nabla)\omega_r$ [Eq. (6b)] and the radial planetary vorticity tilting (PVTr) $P = -2\Omega\partial_\gamma u_r$ [Eq. (6c)], which are scalars since only the

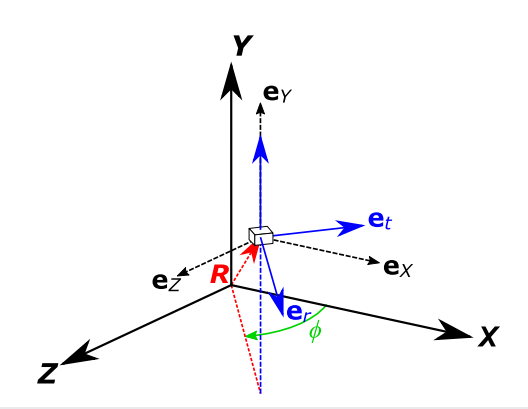


FIG. 5. Definition of the rotated Cartesian frame (t, y, r) using the azimuthal angle ϕ of a fluid particle measured from the fixed Cartesian frame (x, y, z).

radial components are considered,

$$\dot{\omega_r} = -(\mathbf{u} \cdot \nabla)\omega_r + (\boldsymbol{\omega} \cdot \nabla)u_r + \nu \nabla^2 \omega_r + (2\boldsymbol{\Omega} \cdot \nabla)u_r, \quad (6a)$$

$$A = -(\mathbf{u} \cdot \nabla)\omega_r = -(u_t \partial_t + u_y \partial_y + u_r \partial_r)\omega_r, \tag{6b}$$

$$P = (2\mathbf{\Omega} \cdot \nabla) u_r = -2\Omega \partial_{\nu} u_r. \tag{6c}$$

The vorticity advection [Eq. (6b)] represents the transport of radial vorticity by the velocity field **u**. It can be decomposed into three contributions representing the vorticity advection due to tangential u_t , vertical u_v , and radial u_r velocities. Each of these contributions represents the spatial change in radial vorticity due to the difference in each of the velocity components from one point to another. The PVTr is the radial component of the tilting/stretching of planetary vorticity similar to the tilting/stretching of relative vorticity [second term on the right-hand side of Eq. (6a)]. It can be shown that this last term is equivalent to the curl of the Coriolis acceleration,³⁵ which is known from the literature to be critical for maintaining LEV stability and attachment.8,18-20 It is important to briefly point out that the centripetal acceleration has no equivalent term in the vorticity equation [Eq. (4)] since its curl is zero. This is similar to why there is no contribution from the pressure gradient (in incompressible flows), since both terms can be represented as gradients they drop out in the curl. 16 Consider the pressure gradient ∇p and centripetal term $-\mathbf{\Omega} \times (\mathbf{\Omega} \times \mathbf{R}) = \Omega^2 \mathbf{R} = \nabla(\Omega^2 R^2/2)$ from Eq. (3) and note that the curl of any gradient is identically zero $\nabla \times \nabla \varphi = 0$. The other terms in Eq. (6a), such as the time derivative of radial vorticity $\dot{\omega}_r$, the tilting and stretching of vorticity $(\omega \cdot \nabla)u_r$, and the vorticity diffusion $v\nabla^2\omega_r$, are not discussed in detail in this work but have been discussed in the authors' previous work^{27,35} and elsewhere in the literature.3

C. Identification of the quasi-steady period

In the authors' previous work, Werner et al. 35 identified the quasi-steady state by first observing the temporal behaviors of the lift coefficient C_L and the vortex structure over the first three revolutions. The same process is applied here, and more details on the identification of the quasi-steady period can be found in

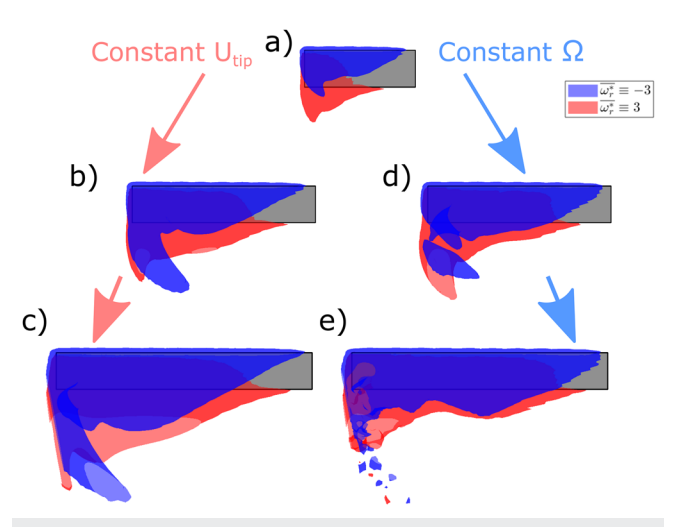


FIG. 6. Normalized time-averaged radial vorticity iso-surfaces $\overline{\omega_r}/2\Omega$: (a) AR = 3, $Re_q = 110$, (b) AR = 5, $Re_q = 110$, (c) AR = 7, $Re_q = 110$, (d) AR = 5, $Re_c = 63.5$ $(Re_q = 183)$, and (e) AR = 7, $Re_c = 63.5$ $(Re_q = 257)$.

supplementary material A. It was determined that the flow had reached an approximately quasi-steady state by the second half of the third revolution of the wing (at 900°) since the time-averaged lift coefficient $\overline{C_L}$ had become roughly constant across all AR and Re_g considered in this study [see Fig. A1(b)]. This is confirmed by the observations of Birch and Dickinson²⁵ who noticed that, by the third stroke, the wake had become fully established at Re typical to insects. Furthermore, others noted that the wake had become fully established after 1.5-2 revolutions by observing the force coefficients at Re between 1500 and ~8000. 3,54,55 Because the temporal features of the flow in this period were much smaller than those at previous time steps based on $\overline{C_L}$, the entire flow was time-averaged during the second half of the third revolution.

Figure 6 shows iso-surfaces of normalized time-averaged radial vorticity $\overline{\omega_r}/2\Omega$ during the quasi-steady period. The LEV controlvolume is comprised of negative radial vorticity (blue) and has a conical shape over the wing surface before shedding from the tip as a tip vortex (TiV) that is roughly aligned in the positive tangential direction (Fig. 5), while the shear layer and trailing-edge vortex (TEV) (red) remain in-between the LEV and the suction side of the wing. In general, the vortex structure for both sets of Reynolds number simulations is very smooth due to the relatively small temporal variations in the vorticity field because of the time-averaging process. However, the LEV control-volume in the constant angular simulations (Rec = 63.5) is not as smooth near the wing-tip where the tip velocity is the largest [Fig. 2(c)]. The TiV is comprised of both negative and positive radial vorticity and tangential vorticity and only forms within approximately one chord length from the wing-tip. 27,31,33 At AR = 5 and Re_g = 183, the time-averaged LEV has shed into two coherent structures [Fig. 6(d)] in the TiV similar but not identical to what has been observed in the literature. 36,56 Additionally, at AR = 7 and $Re_g = 257$ [Fig. 6(e)], the time-averaged LEV has completely deteriorated into small substructures indicating a possibly burst LEV^{5/} and more turbulent flow near the tip due to the higher local Reynolds number Re(r).

D. Averaging methods

The remainder of our analysis focuses on the averaged quantities. Before normalizing the vorticity advection [Eq. (6b)] and PVTr [Eq. (6c)], the flow variables were time-averaged during the quasisteady period. Because the wing is rotating in a fixed grid (although calculations are done in the relative frame) in order to time-average the flow, all of the time intervals for the average need to be collapsed onto a single wing position, so the first time step was chosen corresponding to the initial angle of the wing during the time-averaging period. The overlapping meshes as a result of this process are then spatially averaged along with the flow data onto a single 3D mesh. At this point, the time-averaged LEV was defined using an iso-value of $\overline{\omega_r^*} = \overline{\omega_r}/2\Omega \equiv -3$ (Fig. 6). The radial vorticity was chosen to visualize the LEV instead of the more common Q-criterion ^{58,59} or vorticity magnitude^{31,59} since only radial vorticity dynamics are being considered. We chose this iso-value since it best identified the main structure of the LEV, although it also included a portion of the tip vortex. Different iso-values were tested when defining the control-volume, but these values did not significantly change the results outside of a narrow range of $-4 \lesssim \overline{\omega_r^*} \lesssim -2$. The method for calculating the spatial averages (local \widehat{X} and global \widetilde{X}) is discussed in detail in the Appendix of the authors' previous work,³⁵ but a brief summary of the process is given here.

The local spatial average was calculated as flow variables were spatially averaged on radial slices defined by the region of cylinders centered at the rotation axis [Fig. 7(ii)] within the time-averaged LEV. The flow variables at each of the discrete data points on the grid were interpolated onto a cylindrical slice giving the average variation of each term along the wing-span within the LEV. The global averages were calculated by taking a weighted average of the local spatial averages along the span using the local surface area of the cylinder within the LEV (cross-sectional LEV area) as the weight. It should be noted that a small region of the LEV was removed along the leading-edge due to the extremely high velocity and vorticity gradients. On the content of the content of the cylinder within the content of the cylinder within the LEV (cross-sectional LEV area) as the weight.

E. Scaling methods

In the authors' previous work,³⁵ it was predicted that the vorticity advection [Eq. (6b)] and PVTr [Eq. (6c)] should scale similarly with AR. The original scaling prediction for the vorticity advection and PVTr was developed by considering the work of Lentink and Dickinson⁸ and Cheng et al.²⁷ Previously, the velocity was scaled by the wing speed at the radius of gyration $\mathbf{u}^* = \mathbf{u}/U_g$, the vorticity by the planetary vorticity magnitude $\omega^* = \omega/2\Omega^{17}$ (or twice the wing angular velocity), and the gradients by the wing chord ∇^* = ∇c . This results in an expected scaling for the vorticity advection and PVTr that is proportional to $2\Omega^2 Ro$, which at constant Re_q is inversely proportional to Ro [Eqs. (7a) and (7b)]. When $Re_c =$ 63.5, the values are within the same order of magnitude (Table I). Therefore, assuming that both the normalized vorticity advection and PVTr are approximately O(1) and constant, both the vorticity advection and PVTr should be inversely proportional to *Ro* (or *AR*). However, the authors³⁵ previously demonstrated that the vorticity advection decreased faster than the PVTr with increasing AR from 3 to 7 (maintaining a constant wing chord) at constant Re_g . Therefore, a new normalization needs to be developed that is also consistent with the previous PVTr scaling. Harbig, Sheridan, and Thompson ³⁶ suggested using the span s as the single length scale instead of the chord; however, we will use the radius of gyration r_g here since it is already included in the velocity scale, and it is proportional to the span. Applying the span instead of the chord gives an expected scaling of the vorticity advection and PVTr proportional to $2\Omega^2$, which at $Re_g=110$ is inversely proportional to Ro^2 [Eqs. (7c) and (7d)]. From here onward, we will designate normalized quantities with * if no length scale is specified, whereas *, c is for when the chord is used [Eqs. (7a) and (7b)] and *, s is for when the span is used [Eqs. (7c) and (7d)],

$$A = A^{*,c} 2\Omega^2 Ro \propto A^{*,c} Ro^{-1}, \tag{7a}$$

$$P = P^{*,c} 2\Omega^2 Ro \propto P^{*,c} Ro^{-1}, \tag{7b}$$

$$A = A^{*,s} 2\Omega^2 \propto A^{*,s} Ro^{-2},$$
 (7c)

$$P = P^{*,s} 2\Omega^2 \propto P^{*,s} Ro^{-2}$$
. (7d)

Using the wing-span suggests that both the vorticity advection and PVTr should scale inversely with Ro²; however, the PVTr when normalized using the chord $P^{*,c}$ in Eq. (7b) is already known to be approximately O(1); therefore, when the PVTr is normalized using the span $P^{*,s}$ in Eq. (7d), it is expected to be proportional to Ro, i.e., $P^{*,s} = P^{*,c}Ro \propto Ro$. Similarly, the vorticity advection normalized with the span $A^{*,s}$ can be expected to be approximately O(1) and independent of Ro since the vorticity advection normalized using the chord $A^{*,c}$ is already known to be roughly inversely proportional to Ro. Assuming that both the normalized vorticity advection using the span $A^{*,s}$ [Eq. (7c)] and PVTr using the chord $P^{*,c}$ [Eq. (7b)] are approximately O(1) and independent of AR, two length scales are required to correctly normalize the vorticity advection and PVTr, but also the vorticity dynamics in general. The PVTr has only one spatial gradient [Eq. (6c)] in the vertical direction ∂_{ν} , while the vorticity advection [Eq. (6b)] has three spatial gradients,

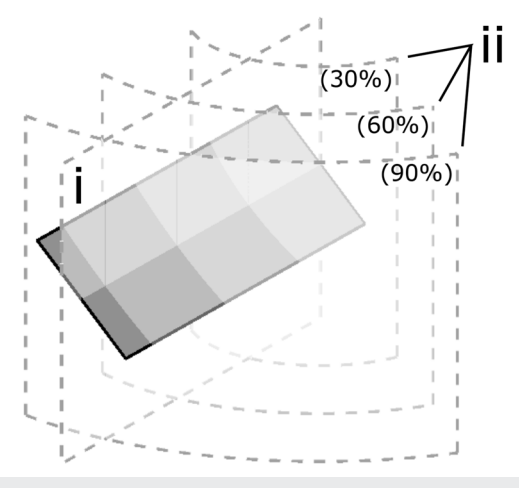


FIG. 7. Schematic showing the locations of slices. (i) Vertical slices cut through the center of the wing. (ii) Selected cylindrical slices at different spanwise positions. The intersection of these cylindrical slices and the LEV control-volume is used to calculate the spatial averages.

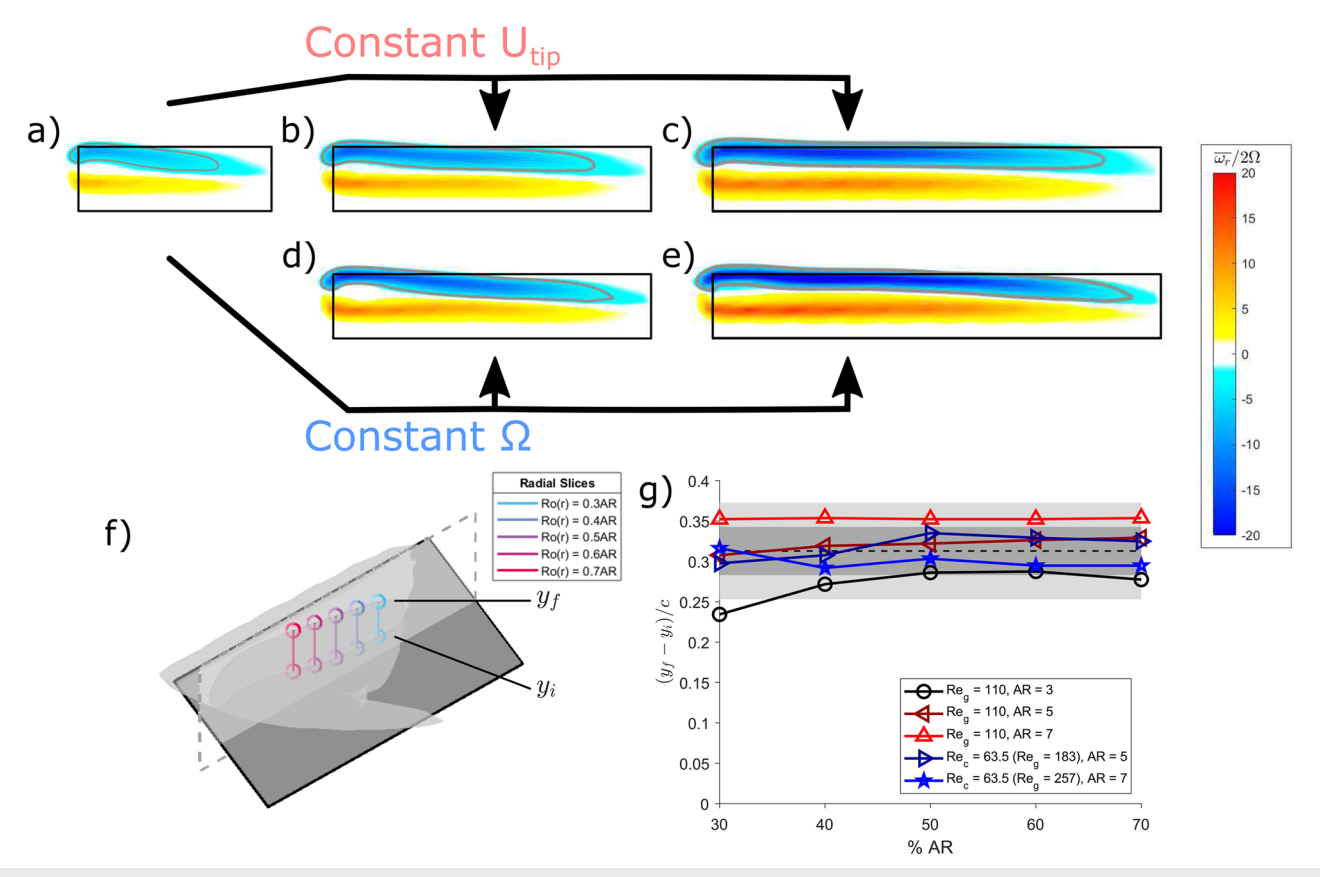


FIG. 8. Vertical slices of the normalized radial vorticity $\overline{w_r}/2\Omega$ showing the wing and LEV, with a gray line for the LEV at $\overline{w_r}^* \equiv -3$: (a) AR = 3, $Re_g = 110$, (b) AR = 5, $Re_g = 110$, (c) AR = 7, $Re_g = 110$, (d) AR = 5, $Re_g = 63.5$ ($Re_g = 183$), and (e) AR = 7, $Re_c = 63.5$ ($Re_g = 257$). (f) and (g) Normalized vertical depth of the time-averaged LEV. (f) Vertical lines through the LEV at the center of the wing at 30%-70% span inside the LEV defined by $\overline{w_r}^* \equiv -3$. These vertical lines are drawn on the vertical plane going through the center of the wing [Fig. 7(i)]. (g) Normalized depth of the LEV ($y_f - y_i$)/c from each case plotted against %AR. The black dashed line represents the mean of all data points, and the dark and light gray regions represent one and two standard deviations above and below the mean, respectively. The black curve represents AR = 3, $Re_g = 110$, while the red curves represent constant U_{tip} and the blue curves represent constant Ω following Fig. 2.

in the tangential ∂_t , vertical ∂_y , and radial ∂_r directions. The single spatial gradient in the PVTr suggests that the vertical direction likely uses the wing chord. Similarly, the remaining two spatial gradients in the vorticity advection should use the span for a length scale.

In order to quantify the scaling of the flow variables with AR, the global averages are modeled using a power law regression of the form $\widetilde{X} = C A R^n$ in MATLAB for a dummy variable X. The power n is restricted to within [-1,1] since the global averages

TABLE II. Aspect-ratio and approximate Re_g for the corresponding span-based Reynolds numbers used from the work of Harbig, Sheridan, and Thompson.³⁶

	$Re_s = 613$	$Re_s = 7667$
AR	R	Le _g
2.91	105	1317
5.1	60.1	752
7.28	42.1	527

do not appear to grow to infinity with increasing AR. Although the range of AR ($3 \le AR \le 7$) used in this analysis is limited, it covers the range primarily found in insects and other flying animals. 8,13 We argue that because this range encompasses the majority of ARs in nature, it is adequate to quantify the primary scaling of vorticity dynamics with AR. This nonlinear regression process is applied to the global averages of vorticity advection and PVTr, along with the kinematic flow variables that comprise both such as the radial vorticity ω_r and the three velocity components. Inserting the regression results for these constituent global average variables into the definitions of the vorticity advection allows us to make predictions as to how the tangential, vertical, and radial advections scale individually with AR.

III. RESULTS AND DISCUSSION

A. Two independent LEV length scales

Earlier, it was suggested that two length scales should be used instead of a single scale. The motivation for this comes from the

definition of the PVTr [Eq. (6c)], the vorticity advection [Eq. (6b)], and the predicted scaling of the normalized terms, respectively [Eqs. (7b) and (7c)]; specifically, the vertical direction should scale with the chord and the radial and tangential directions should scale with the span. The use of two length scales is not foreign in the literature; Blasius and Prandtl^{16,61} used the depth of the boundary layer and the wing chord to scale the vertical and streamwise coordinates, respectively, for the flow over a flat plate. Therefore, it seems reasonable that a highly three-dimensional flow structure like the LEV might also be governed by multiple length scales. The radial vorticity of the LEV forms a conical structure growing along the wing-span before being tilted into the wake near the tip. Furthermore, as AR increases with the wing-span (with the chord length fixed), the LEV maintains its conical structure and stretches in the tangential direction with the cross-sectional area (\mathscr{A}_{LEV}) increasing along the span. Here, the cross-sectional area increases uniformly along the span until reaching the tip due to more three-dimensional effects associated with the tip vortex meaning that the radial direction clearly scales with the span. The appropriate scale for the vertical and tangential directions is now discussed.

1. Vertical direction

The vertical depth of the LEV is roughly constant and independent of AR and Re_g . Figures 8(a)–8(e) show vertical slices with normalized time-averaged radial vorticity $\overline{\omega_r}/2\Omega$ contours [Fig. 7(i)].

As AR increases [reading Figs. 8(a)-8(e) from left to right], it appears that the vertical depth of the LEV remains constant along the span and is of the same order of magnitude across AR and Reg. Furthermore, as Reg increases at the same AR [Figs. 8(b) and 8(d), or Figs. 8(c) and 8(e)] or at different ARs [Figs. 8(a) and 8(d), or Fig. 8(e)], the vertical depth of the LEV is also roughly constant along the span. It is possible that there is a minimum threshold that the chord must exceed in order to achieve this constant depth of the LEV, but it is unclear whether this feature is universal in all revolving wing flows or merely those with wing chords of this size. Figure 8(f) shows vertical lines along the vertical slice plane with circles representing the top y_i and bottom y_i of the LEV. Figure 8(g) plots the vertical depth $y_f - y_i$ vs %AR (or % of the wing-span). The vertical depth is roughly constant from 30% to 70% of the span since the majority of the points fall within one standard deviation from the mean (dark gray) except for some locations at AR = 3 and AR = 7 at $Re_g = 110.$

The observation that the depth of the conical LEV is independent of AR and Re_g can also be shown in the literature. Harbig, Sheridan, and Thompson³⁶ visualized the LEV contour at 50% of the wing-span where it can be seen that the depth of the LEV bisected through the center of the wing is roughly constant at different ARs (where the chord was changed while maintaining a constant span) although they did not make specific mention of this. Their wings revolved at the span-based Reynolds number $Re_s = 613$ or 7667 for

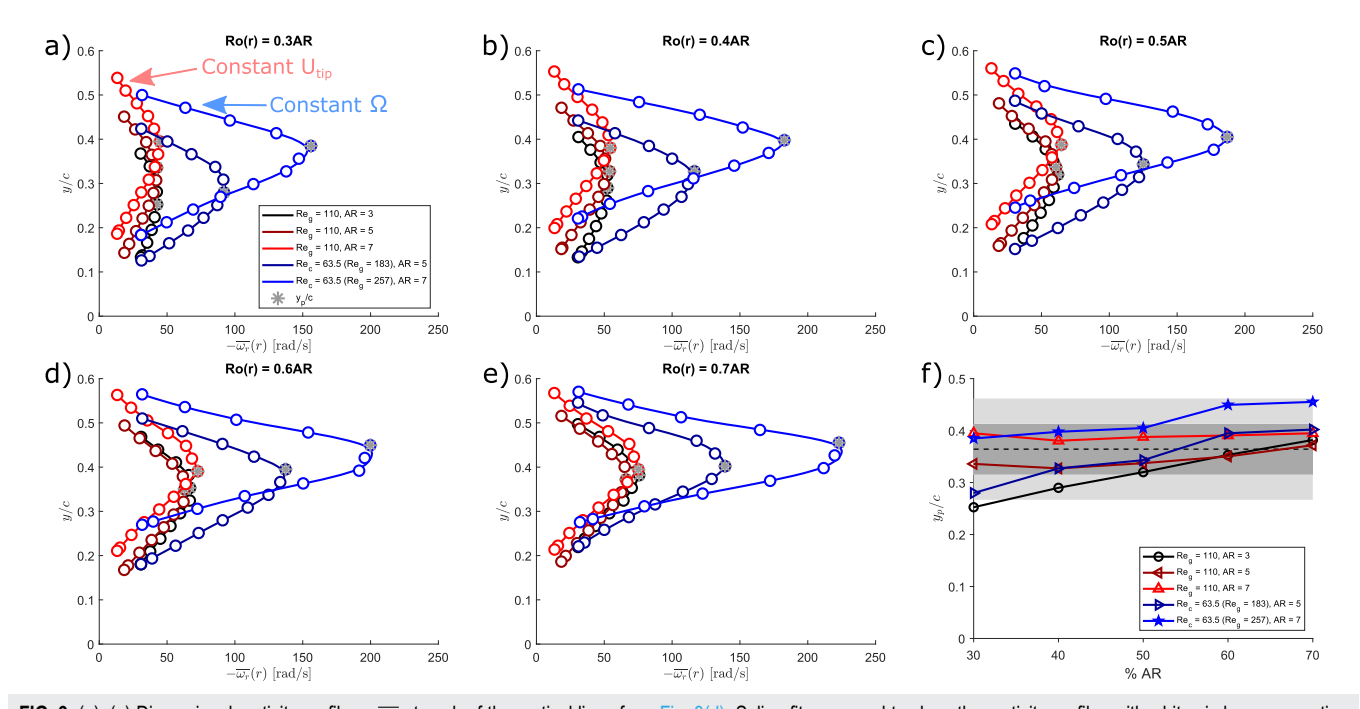


FIG. 9. (a)–(e) Dimensional vorticity profiles $-\overline{\omega_r}$ at each of the vertical lines from Fig. 8(d). Spline fits are used to show the vorticity profiles with white circles representing select data points. The gray * represents the normalized vertical position of the peak y_p/c in the vorticity profiles used in Fig. 9(f): (a) 30%AR, (b) 40%AR, (c) 50%AR, (d) 60%AR, and (e) 70%AR. In (a)–(f), the black curves represent AR = 3, $Re_g = 110$, while the red curves represent constant U_{tip} and the blue curves represent constant Ω following Fig. 2. (f) Normalized vertical position of the peak in the radial vorticity profile. The black dashed line represents the mean of all data points, and the dark and light gray regions represent one and two standard deviations above and below the mean, respectively.

AR = s/c = 2.91, 5.1, and 7.28; the approximate Re_g values at each AR are given in Table II using $Re_g = \frac{Re_s}{AR} \left(\frac{r_g}{s} \right)$, where $r_g/s \approx 0.5$. These corresponding Re_g values were all within the laminar flow regime common in most small flying insects, 10,11,62 so the three-dimensional effects are expected to be mostly negligible except near the tip similar to the flows analyzed in this study. This feature of the LEV is also substantiated by observing the flow structures elsewhere in the literature for revolving 43,44 and flapping 45,46 wings over similar ranges of AR and Re.

Finally, Figs. 9(a)-9(e) show the radial vorticity profiles along the vertical lines [Fig. 8(f)] at different %AR. The vertical location of the peaks in the vorticity profile for each AR and Re_g are in general agreement despite the magnitude increasing along the span and with AR and Re_g . Figure 9(f) shows the vertical location of the peaks y_p normalized by the chord. The location of the peaks increases monotonically in all cases; however, the most extreme values are still within two standard deviations from the mean (except for AR = 3 at $Re_g = 110$ at 30%). Therefore, the variation in the vorticity along the vertical direction is minimal since all of the

variation roughly occurs in the same vertical range. This is a good reason to suggest that either the chord or possibly the average LEV depth (which may be a function of Re_g and AoA) is better choice of length scale for the vertical direction. In this study, since we have not rigorously investigated how LEV depth varies with other parameters, we will continue using the wing chord as the vertical length scale instead.

2. Tangential direction

As was mentioned previously, the LEV stretches to match the different ARs and the cross-sectional area (\mathscr{A}_{LEV}) increases in order to maintain the conical structure of the LEV [Fig. 10(a)], indicating that the radial direction scales with the span. The length scale for the tangential direction follows from this because of how the geometry of the LEV cross-sectional area changes along the span increasing in the tangential direction. Figures 10(b)-10(d) show plots of the cross-sectional area of the LEV from the time-averaged flow with three separate normalization schemes vs the local Rossby number Ro(r) for different ARs and Re_g . Since the LEV cross-sectional area

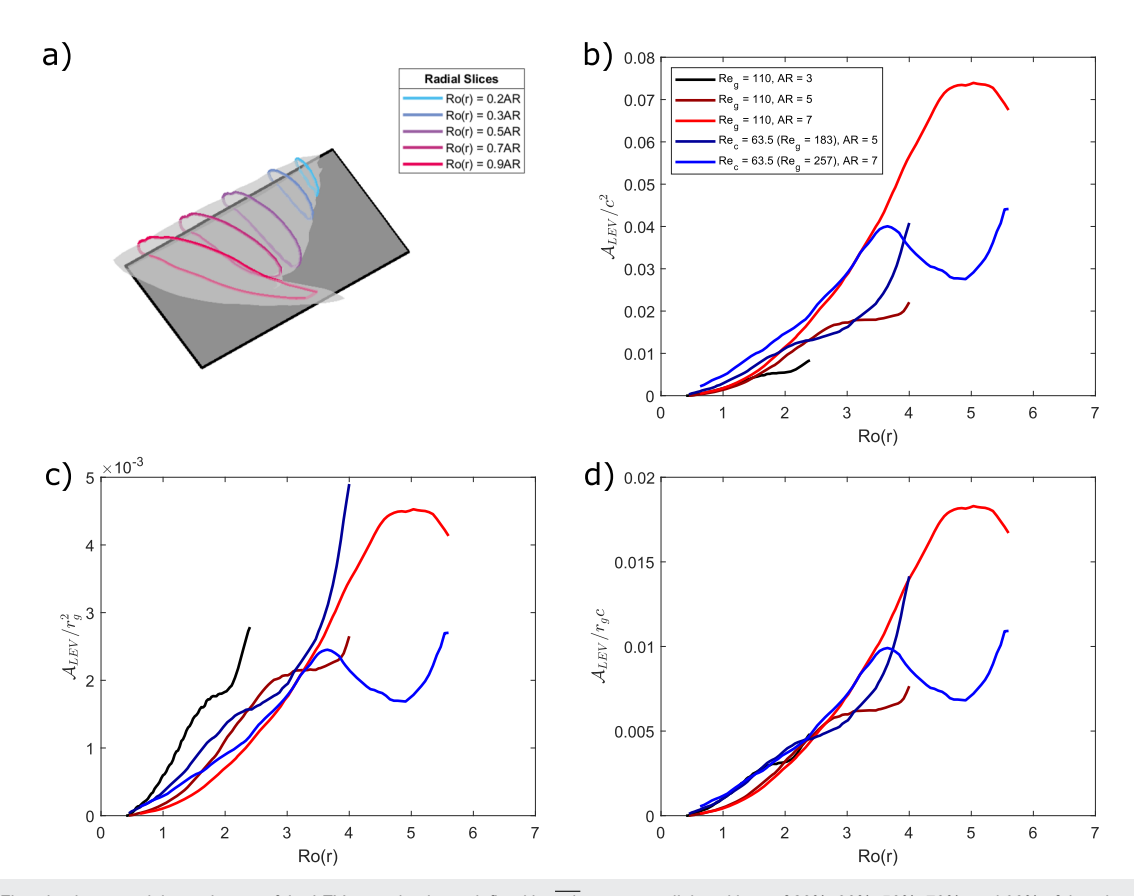


FIG. 10. (a) Five circuits around the perimeter of the LEV control-volume defined by $\overline{\omega_r^*} \equiv -3$ at radial positions of 20%, 30%, 50%, 70%, and 90% of the wing-span and the LEV defined for AR = 3 and $Re_g = 110$. The region after 80% of the wing-span is not considered in evaluating the LEV cross-sectional areas. The circuit used to calculate the local cross-sectional area of the LEV \mathscr{A}_{LEV} is defined at the intersection of cylindrical slices [Fig. 7(iii)] and the LEV control-volume. (b)–(d) Different normalized cross-sectional areas of the LEV \mathscr{A}_{LEV} plotted against the local Rossby number. The black curves represent AR = 3, $Re_g = 110$, while the red curves represent constant U_{tip} and the blue curves represent constant Ω following Fig. 2. (b) $\mathscr{A}_{LEV}^{*,c} = \mathscr{A}_{LEV}/c^2$ using the chord, (c) $\mathscr{A}_{LEV}^{*,s} = \mathscr{A}_{LEV}/r_g^2$ using the radius of gyration, and (d) $\mathscr{A}_{LEV}^{*,sc} = \mathscr{A}_{LEV}/r_g c$ using both the chord and radius of gyration.

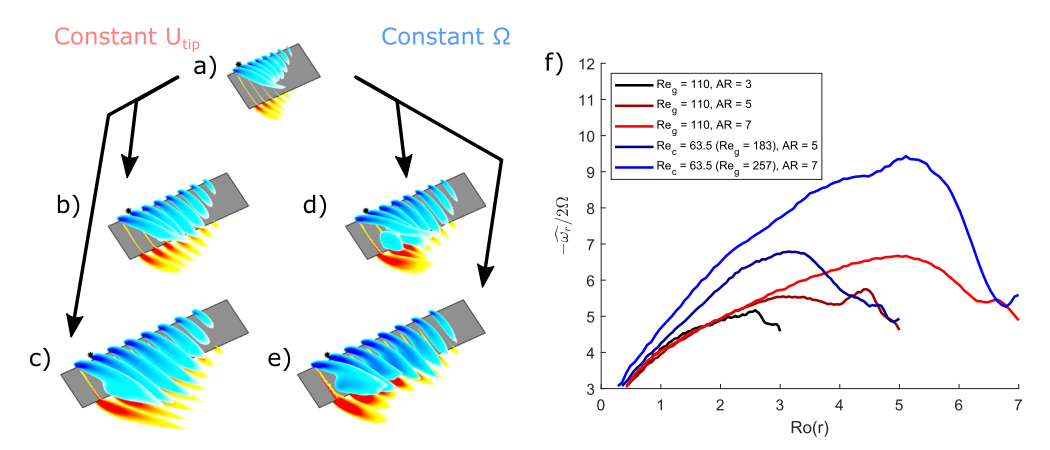


FIG. 11. (a)–(e) Cylindrical slices [Fig. 7(ii)] of normalized radial vorticity along the span $\overline{w_r}/2\Omega$ at radial positions of 20%–90% span; * is shown at 80% span where the LEV is observed to begin lifting off. (a) AR = 3, $Re_g = 110$, (b) AR = 5, $Re_g = 110$, (c) AR = 5, $Re_c = 63.5$ ($Re_g = 183$), (d) AR = 7, $Re_g = 110$, (e) AR = 7, $Re_c = 63.5$ ($Re_g = 183$), and (f) normalized spatial-averaged radial vorticity $-\widehat{w_r}/2\Omega$ within the LEV control-volume (Fig. 6, $\overline{w_r} = -3$) plotted against the local Rossby number. The vorticity was chosen instead of the circulation Γ since the normalization would change depending on if the velocity or vorticity definition was used. The black curves represent $RR_g = 110$, while the red curves represent constant $RR_g = 110$, while the red curves represent constant $RR_g = 110$, while the red curves represent constant $RR_g = 110$, while the red curves represent constant $RR_g = 110$, while the red curves represent constant $RR_g = 110$, while the red curves represent constant $RR_g = 110$, while the red curves represent constant $RR_g = 110$, while the red curves represent constant $RR_g = 110$, while the red curves represent constant $RR_g = 110$, while the red curves represent constant $RR_g = 110$, while the red curves represent constant $RR_g = 110$, while the red curves represent constant $RR_g = 110$, while the red curves represent constant $RR_g = 110$, while the red curves represent constant $RR_g = 110$, while the red curves represent constant $RR_g = 110$, while the red curves represent constant $RR_g = 110$, while the red curves represent constant $RR_g = 110$, while the red curves represent constant $RR_g = 110$, while the red curves represent $RR_g = 110$, while the red curves represent $RR_g = 110$, while the red curves represent $RR_g = 110$, while $RR_g = 110$, where RR_g

is essentially elliptical, it must necessarily use two length scales (not necessarily separate), one corresponding to the tangential direction and another to the vertical.

We first investigate various normalizations of the crosssectional area to better isolate AR and Re_g effects similar to Carr, DeVoria, and Ringuette's study where they normalized the circulation Γ locally along the wing-span. ⁶³ Here, three normalizations are tested, the cross-sectional area $\mathscr{A}_{LEV}^{*,c} = \mathscr{A}_{LEV}/c^2$ using the chord [Fig. 10(b)], $\mathscr{A}_{LEV}^{*,s} = \mathscr{A}_{LEV}/r_g^2$ using the radius of gyration (for the span) as proposed by Harbig, Sheridan, and Thompson³⁶ [Fig. 10(c)], and $\mathscr{A}_{LEV}^{*,sc} = \mathscr{A}_{LEV}/r_gc$ using both [Fig. 10(d)]. The normalization that best collapses the curves of the LEV cross-sectional area along the span is indicative of the appropriate length scale to be used for the tangential direction. In Fig. 10(b), curves of the normalized cross-sectional area $\mathscr{A}_{LEV}^{\star,c}$ using the chord are more vertically displaced at separate ARs. Similarly, in Fig. 10(c), the curves of $\mathscr{A}_{LEV}^{*,s}$ using the radius of gyration show more disparity between ARs along the local Rossby number axis. Neither of these normalizations fully collapse the curves; however, the curves of $\mathscr{A}_{LEV}^{\star,sc}$ using both the chord and radius of gyration in Fig. 10(d) all roughly collapse onto each other. Knowing that the vertical direction scales with the chord since the depth of the LEV is roughly constant and that the third normalization $\mathscr{A}_{LEV}^{\star,sc}$ successfully collapses each curve, the tangential direction must scale with the radius of gyration (or the span) similar to the radial direction. This makes sense of the observed stretching of the LEV in the tangential direction with increasing AR.

Lastly, the tangential direction can also be shown to scale in the same manner as the radial direction by considering the definition of the coordinates in the rotated Cartesian system and motion of the wing-tip. Starting from Eq. (5), the tangential direction is defined as $t = \sin(\phi)x + \cos(\phi)z$ and the radial direction as $r = \cos(\phi)x - \sin(\phi)z$. Taking the derivative of t with respect to ϕ gives $dt = (\cos(\phi)x - \sin(\phi)z)d\phi$ or $dt = rd\phi$. This suggests that a change in the tangential direction is directly proportional to the radial position assuming a constant sweep angle $d\phi$. As the wing rotates,

the wing-tip sweeps out a circular arc that is proportional to the span corresponding to the relationship derived just above. This indicates the length scale that is used for the tangential direction is identical to what is used for the radial in agreement with the argument from the LEV geometry.

B. Three-dimensional effects and geometric-similarity

So far in this work, the time-averaged flow in the LEV controlvolumes (Fig. 6) has been treated as being entirely two-dimensional. However, the presence of the tip vortex creates a region that is highly three-dimensional compared to the main LEV. In Figs. 11(a)-11(e), the radial vorticity is attached to the wing until ~80% of the span (shown by *) before detaching and shedding, forming the tip vortex. Additionally, some cases begin to show signs of recirculation [Fig. 11(c)], at $Re_g = 110$ and at $Re_c = 63.5$ [Figs. 11(d) and 11(e)] corresponding to the higher AR and $Re_g \ge 110$ (Table I). Figure 11(f) shows the spatially averaged normalized radial vorticity $-\widehat{\omega}_r/2\Omega$ increasing monotonically until reaching ~1.5 chord lengths from the tip, agreeing with the observations of Jardin, Farcy, and David³³ and DeVoria and Mohseni. 34 In the three-dimensional region, the trend in the radial vorticity is distinct from that in the two-dimensional region decreasing due to the reduced radial vorticity and is likely a result of the tilting term in Eq. (6a).³⁵ A similar abrupt change is observed in velocity components, vorticity advection, and PVTr.

The three-dimensional effects can also be understood in terms of geometric-similarity, where we define a region to be geometrically similar if the flow profiles at different radial positions are similar in shape. In this analysis, we will consider the profiles that are within one standard deviation from the mean to be geometrically similar to each other, whereas those outside to be geometrically dissimilar due to three-dimensional effects. To this end, we calculate a simple geometric-similarity metric (GSM), which is the percentage of the local flow profile that extends either above or below one standard deviation from the mean profile. This geometric-similarity metric is plotted vs % AR in Fig. 12 for each of the six flow variables for each AR and Reg combination. From Fig. 12,

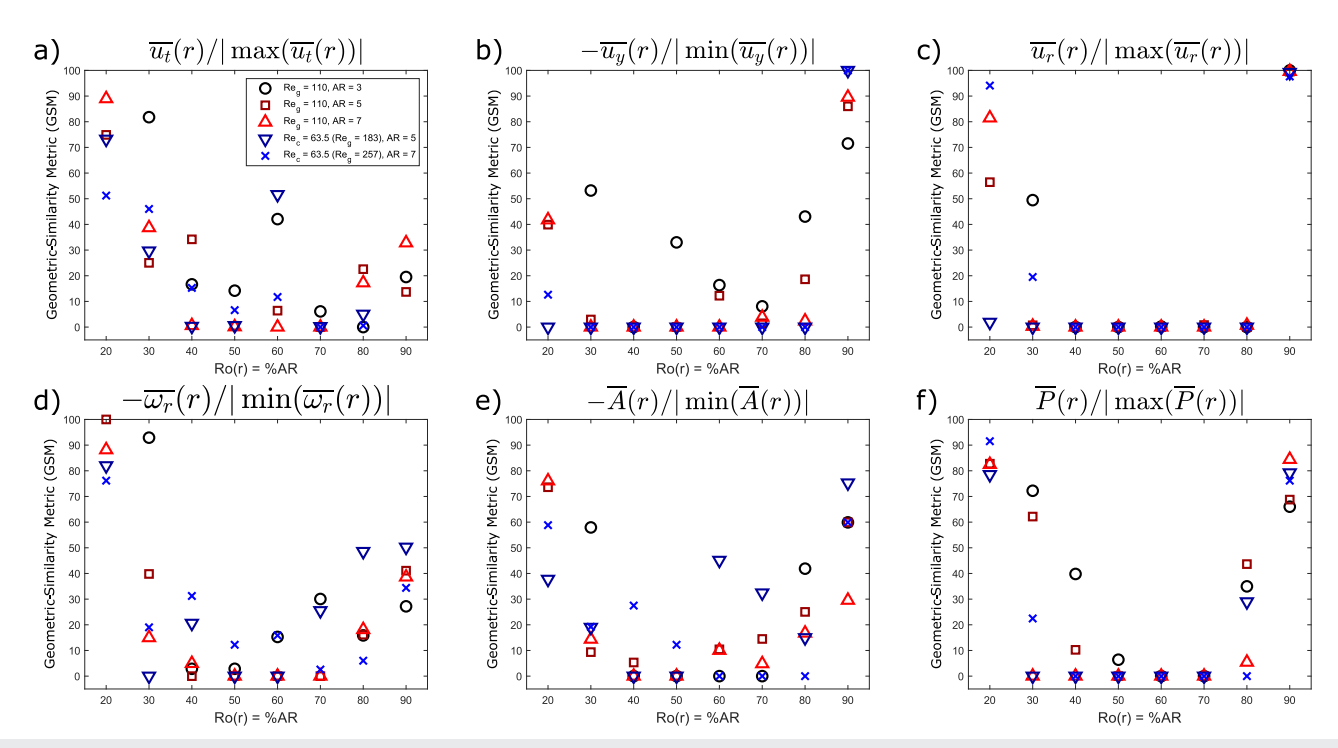


FIG. 12. Geometric-similarity metric (GSM) of normalized flow profiles: (a) tangential velocity $\overline{u_t}(r)/|\max(\overline{u_t}(r))|$ (Fig. B1), (b) vertical velocity $-\overline{u_y}(r)/|\min(\overline{u_y}(r))|$ (Fig. B2), (c) radial velocity $\overline{u_r}(r)/|\max(\overline{u_r}(r))|$ (Fig. B3), (d) radial vorticity $-\overline{w_r}(r)/|\min(\overline{w_r}(r))|$ (Fig. B4), (e) vorticity advection $-\overline{A}(r)/|\min(\overline{A}(r))|$ (Fig. B5), and (f) PVTr $\overline{P}(r)/|\max(\overline{P}(r))|$ (Fig. B6). The GSM is the percentage of the local flow profile that extends past one standard deviation from the mean for each of the separate cases: AR = 3, $Re_g = 110$; AR = 5, $Re_g = 110$; AR = 5, $Re_c = 63.5$ ($Re_g = 183$); AR = 7, $Re_g = 110$; and AR = 7, $Re_c = 63.5$ ($Re_g = 257$).

the trend that emerges is that generally, the regions near the root $[Ro(r) \lesssim 0.4AR]$ and tip $[Ro(r) \gtrsim 0.8AR]$ are less geometrically similar having a higher GSM, whereas the central region of the LEV is more geometrically similar having a GSM at or near

Therefore, the regions that are not geometrically similar should be removed from the analysis because of the stronger threedimensional effects. This is done by removing percentages of the LEV control-volume starting from the root and/or the tip moving toward the center of the wing based on calculating the coefficient of determination R^2 using power law regressions [see Eq. (8)]. This process involves simultaneously maximizing R^2 while minimizing the total percentage of the LEV control-volume removed from both sides of the wing. The coefficients of determination are considered to be functions of the percent of the LEV control-volume removed and are expected to increase until the contributing three-dimensional features are removed. These and the resulting global averages of the different flow variables are both discussed in supplementary material B.

C. Global scaling arguments of flow variables applied to vorticity advection

At this point, we have discussed why two length scales are needed to correctly normalize the LEV vorticity dynamics, along with the characteristic magnitudes of the velocity and vorticity. Recall from earlier that these characteristic magnitudes are the

velocity at the radius of gyration U_g for the velocity and the planetary vorticity magnitude 2Ω for the vorticity. Additionally, the length scale that is predicted to best normalize the vorticity advection is the span s (or radius of gyration r_g), while the length scale that correctly normalizes the PVTr is the chord c. Figure 13 shows the application of these two length scales using the global vorticity advection \widetilde{A} and PVTr \widetilde{P} following Eq. (7) and power law regressions. The values using the chord as the characteristic length are in good agreement with those in the authors' previous work³⁵ as expected. The normalized global vorticity advection $\tilde{A}/2\Omega^2 Ro$ [Eq. (7a)] varies roughly inversely with increasing AR [Fig. 13(a)], while the PVTr $\widetilde{P}/2\Omega^2 Ro$ [Eq. (7b)] is approximately independent of AR [Fig. 13(b)] and Table B3], indicating that the chord should be used as the length scale in normalizing the PVTr but not the vorticity advection. Conversely, taking the wing-span as the single length scale as proposed by Harbig, Sheridan, and Thompson³⁶ gives a normalized global vorticity advection $\tilde{A}/2\Omega^2$ [Eq. (7c)] that is roughly constant [Fig. 13(c)]. Additionally, the power χ used for the global averages of vorticity advection [Eq. (8e)] is approximately zero [see Fig. B6(b) and Table B3] as predicted. At the same time, though, the PVTr $\widetilde{P}/2\Omega^2$ [Eq. (7d)] is roughly linearly increasing [Fig. 13(d)], suggesting that the wing-span is a better choice to use for the vorticity advection but not the PVTr. Therefore, the anisotropic characteristic length scales based on the LEV geometry successfully predicted the scaling of vorticity advection and PVTr.

Notably, in Fig. 13(c), the global averages of vorticity advection are lower at AR = 7 than the other cases. This can primarily

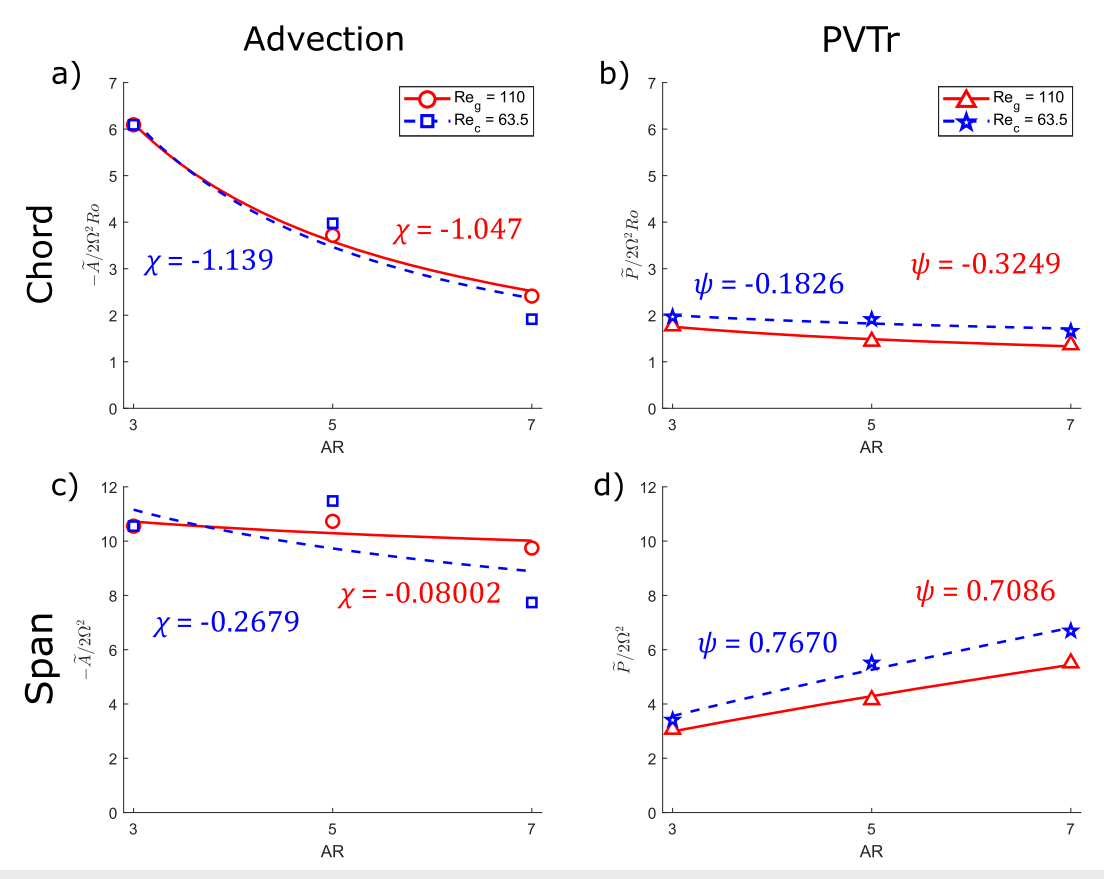


FIG. 13. Normalized vorticity advection and PVTr using both proposed length scales from Eq. (7). The red curves and data points represent constant U_{tip} , while the blue dashed curves and data points represent constant Ω following Fig. 2. (a) Vorticity advection using the chord: $-\widehat{A}^{*,c} = -\widetilde{A}/2\Omega^2 Ro$. (b) PVTr using the chord: $\widehat{P}^{*,c} = \widetilde{P}/2\Omega^2 Ro$. (c) Vorticity advection using the span: $-\widehat{A}^{*,c} = -\widetilde{A}/2\Omega^2$. (d) PVTr using the span: $-\widehat{P}^{*,c} = -\widetilde{P}/2\Omega^2$. (a) and (c) Circles represent $-\widehat{R}^{*}$ = 110 and squares represent $-\widehat{R}^{*}$ = 110 and stars represent $-\widehat{R}^{*}$ = 63.5 for vorticity advection. (b) and (d) Triangles represent $-\widehat{R}^{*}$ = 110 and stars represent $-\widehat{R}^{*}$ = 63.5 for PVTr.

be accounted for by the fact that the vorticity advection is made up of three separate contributions associated with the tangential, vertical, and radial directions. In other words, it is more consistent for the vertical advection to have the chord as its length scale, while the tangential and radial advections should use the span. To better understand the individual contributions of the tangential, vertical, and radial advections to the vorticity advection, we derived scaling relationships for each by combining the nonlinear regression equations based on the individual velocity components [Eqs. (8b)–(8d)] and the radial vorticity [Eq. (8a)]. Additionally, power law regressions for the vorticity advection [Eq. (8e)] and PVTr [Eq. (8f)] are also derived. Greek letters are used for the powers and subscripts for the leading coefficients, and each global variable is normalized so that the effect of the characteristic magnitudes for the velocity and vorticity and length scale does not artificially affect the coefficients,

$$\widetilde{\omega_r^*} = \frac{\widetilde{\omega_r}}{2\Omega C_\alpha A R^\alpha},\tag{8a}$$

$$\widetilde{u_t^*} = \frac{\widetilde{u_t}}{U_\sigma C_\beta A R^\beta},\tag{8b}$$

$$\widetilde{u_y^*} = \frac{\widetilde{u_y}}{U_g C_\gamma A R^\gamma},\tag{8c}$$

$$\widetilde{u_r^*} = \frac{\widetilde{u_r}}{U_g C_\delta A R^\delta},\tag{8d}$$

$$\widetilde{A^{*,s}} = \frac{\widetilde{A}}{2\Omega^2 C_v A R^{\chi}},\tag{8e}$$

$$\widetilde{P^{*,c}} = \frac{\widetilde{P}}{2\Omega^2 RoC_{\psi} A R^{\psi}}.$$
 (8f)

Starting from the definition of the vorticity advection [Eq. (6b)] and normalizing using the established length scales and characteristic magnitudes, we insert the scaling equations for the vorticity and velocity components [Eqs. (8a)–(8d)]. This procedure is the same as what is discussed by Kundu and Cohen¹⁶ regarding the boundary layer approximation. They start with the Navier–Stokes equations and insert the characteristic magnitudes for the different velocity

components and the length scales for the gradients to arrive at relationships that describe the order of each term. For example, the tangential velocity $\widetilde{u}_t = U_g(C_{\beta}AR^{\beta})\widetilde{u}_t^*$ [Eq. (8b)] is used in the tangential advection along with the radial vorticity [Eq. (8a)] and the

span for the tangential length scale. This gives combined coefficients and powers that allow for the prediction of relative magnitudes and variation with respect to AR for each advection term. The process for all three advection terms is shown in the following equation:

$$\widetilde{A^{*,s}} = \frac{\widetilde{A}}{2\Omega^{2}} = -\frac{1}{2\Omega^{2}} \left[\widetilde{u_{t}} \frac{\partial \widetilde{\omega_{r}}}{\partial t} + \widetilde{u_{y}} \frac{\partial \widetilde{\omega_{r}}}{\partial y} + \widetilde{u_{r}} \frac{\partial \widetilde{\omega_{r}}}{\partial r} \right] = -\frac{1}{2\Omega^{2}} \left[C_{\alpha} C_{\beta} \left(\frac{U_{g} A R^{\beta} 2 \Omega A R^{\alpha}}{s} \right) \widetilde{u_{t}^{*}} \frac{\partial \widetilde{\omega_{r}^{*}}}{\partial t^{*,s}} + C_{\alpha} C_{\gamma} \left(\frac{U_{g} A R^{\gamma} 2 \Omega A R^{\alpha}}{c} \right) \widetilde{u_{y}^{*}} \frac{\partial \widetilde{\omega_{r}^{*}}}{\partial y^{*,c}} \right] + C_{\alpha} C_{\delta} \left(\frac{U_{g} A R^{\delta} 2 \Omega A R^{\alpha}}{s} \right) \widetilde{u_{r}^{*}} \frac{\partial \widetilde{\omega_{r}^{*}}}{\partial r^{*,s}} \right] = - \left[C_{t} \left(A R^{\alpha+\beta} \right) \widetilde{u_{t}^{*}} \frac{\partial \widetilde{\omega_{r}^{*}}}{\partial t^{*,s}} + C_{y} \left(A R^{\alpha+\gamma+1} \right) \widetilde{u_{y}^{*}} \frac{\partial \widetilde{\omega_{r}^{*}}}{\partial y^{*,c}} + C_{r} \left(A R^{\alpha+\delta} \right) \widetilde{u_{r}^{*}} \frac{\partial \widetilde{\omega_{r}^{*}}}{\partial r^{*,s}} \right]. \tag{9}$$

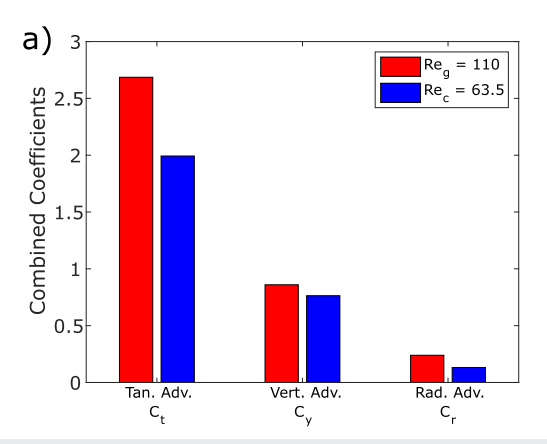
The combined coefficients and 95% confidence intervals are tabulated in Table III, and the method for calculating them starting from the original coefficients is discussed in supplementary material B. From examination of Eq. (6b), it is expected that each of the individual contributions to the vorticity advection should all be of the same order as the vorticity advection. Since the vorticity advection normalized using the span $\widehat{A^{*,s}} = \widehat{A}/2\Omega^2$ is expected to be roughly of order one across the different ARs as a consequence of our normalization, the same can be assumed for the individual contributions in Eq. (9). Since each of the individual terms will be of order one as a consequence of our normalization, their products and derivatives should as well. Therefore, it can be reasoned that the relative size of each normalized vorticity advection term in Eq. (9) is determined by the presence of a multiplying factor involving AR.

It is still relevant to consider their relative magnitudes before addressing the combined powers (Table III). Clearly, the tangential advection C_t is the largest of the three, followed by the vertical C_y and then the radial C_r , which is actually an order of magnitude smaller than the others [see Fig. 14(a)]. This is in good agreement with that reported in the literature. Cheng et al. Toted that the tangential and vertical advections were both much larger than the radial advection, which was essentially negligible at similar Re_g to those considered in this study. Chen, Wu, and Cheng also observed that during the developmental phase of the LEV, the tangential advection was largest, followed by the vertical and then the radial, which they also noted to be negligible.

Figure 14(b) shows the combined and total powers for the vorticity advection. In general, the level of agreement between the combined and total powers (which are $\chi \approx 0$) indicates the relative strength of the individual terms in the vorticity advection as AR changes. The combined power for the tangential advection $(\alpha + \beta)$ and the total power χ are both approximately zero. For $Re_g = 110$, both powers are of the same sign, while the signs are different for Re_c = 63.5. Since the tangential advection power is approximately zero, this indicates that the tangential advection is relatively invariant with AR. On the other hand, the vertical $(\alpha + \gamma + 1)$ and radial $(\alpha + \delta)$ combined powers are an order of magnitude larger. This indicates that in the limit of $AR \rightarrow \infty$, both the vertical and radial advections will increase. However, from Fig. 14(a), it is seen that the tangential advection is still likely to be the dominant term at larger ARs since $C_t \ge C_y$ and $C_t \gg C_r$. This coincides with Lentink's observation that revolving wings of higher ARs approximate translating wings. The vorticity advection associated with translating wings is primarily chordwise oriented or in the tangential direction and is the main source of vorticity transported into the boundary layer. However, it should be noted that Han, Chang, and Cho³² observed that the downwash varied inversely with AR for revolving wings at Re, an order of magnitude larger than those used in this study. Since our simulations were all at constant or approximately constant Reg across the different ARs, this could suggest that the downwash varies inversely with Reg, but this was not investigated here. It is known that revolving or flapping wings with smaller ARs exhibit more

TABLE III. Combined coefficients (absolute value) and 95% confidence intervals in parenthesis for the tangential, vertical, and radial advections for Re_g = 110 and Re_c = 63.5. The method for calculating these coefficients and confidence intervals is discussed in supplementary material B.

	$\widetilde{u_t^*} \Big(\partial \widetilde{w_r^*} / \partial t^{*,s} \Big)$		$\widetilde{u_y^*}\Big(\partial \widetilde{u_r^*}/\partial y^{*,c}\Big)$		$\widetilde{u_r^*}\Big(\partial \widetilde{w_r^*}/\partial r^{*,s}\Big)$	
	C_t	$\alpha + \beta$	C_y	$\alpha + \gamma + 1$	C_r	$\alpha + \delta$
$Re_g = 110$	2.686 (-15.61, 20.98)	-0.1264 ($-2.403, 2.150$)	0.8598 (-1.647, 3.336)	1.025 (0.09799, 1.952)	0.2394 (-0.4898, 0.9686)	0.7176 (-1.559, 2.994)
$Re_c = 63.5$	1.993 (—13.02, 17.01)	0.0867 (-2.126, 2.299)	0.7636 (-14.11, 15.63)	$1.121 \\ (-1.911, 4.153)$	0.1317 (-3.307, 3.571)	1.317 (-2.776, 5.410)



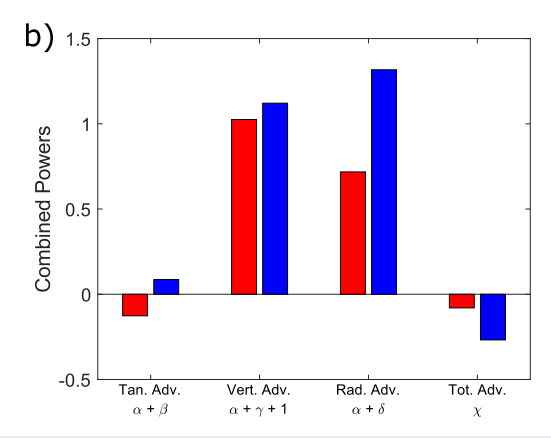


FIG. 14. Bar graph showing (a) the combined leading coefficients (absolute value) and (b) the combined and total powers for the vorticity advection. Red bars represent constant U_{tip} , and blue bars represent constant Ω following Fig. 2. (a) Tangential C_t , vertical C_y , and radial C_t advection coefficients. (b) Tangential $\alpha + \beta$, vertical $\alpha + \gamma + 1$, radial $\alpha + \delta$, and vorticity α advection powers.

three-dimensional flow mechanisms on top of the main tangential flow, which is in agreement with what we have observed.

D. Additional observations: Global scaling application and localized exceptions

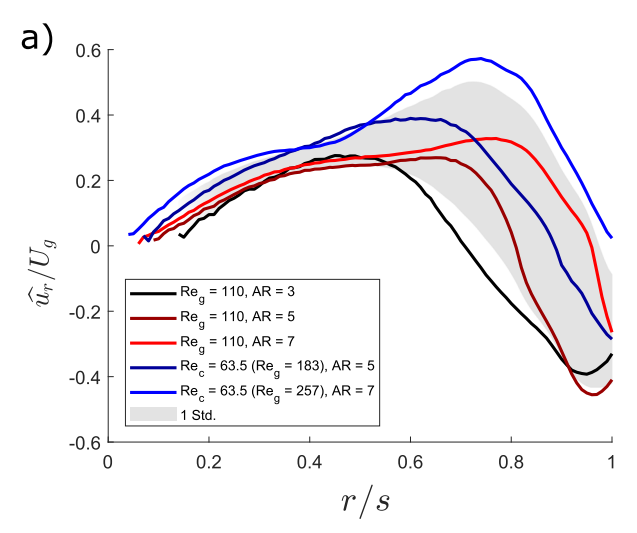
In Sec. III C, but also Secs. II E and III A, we describe additional details regarding the application of the scaling of the vorticity dynamics in previous sections. This scaling is described in Eq. (8) from Sec. III C, that is, the terms in the denominators except the power law relations. The radial vorticity [Eq. (8a)] was normalized by the planetary vorticity magnitude 2Ω and all three velocity components [Eqs. (8b)–(8d)] by the velocity of the wing at the radius of gyration U_g . Next, the vorticity advection [Eq. (8e)] was normalized by $2\Omega^2$ since the span was used as the length scale [Eq. (7c)]. Finally, the PVTr [Eq. (8f)] was normalized by $2\Omega^2 Ro$ due to the chord being used for the length scale in the gradient [Eq. (7b)]. The inclusion of the power law relations in the denominator of the normalized vorticity dynamics equations allows us to quantify the accuracy of these scaling terms in predicting the global behavior of the vorticity dynamics (these powers are provided in supplementary material B: Table B3). If the power is approximately zero, then the original scaling term accurately represents the global variation across AR at constant Re_g typical to insect flight. This applies to the global advection $\widetilde{A}^{*,s}$ [Fig. 13(c)] and PVTr $\widetilde{P}^{*,c}$ [Fig. 13(b)]. Contrastingly, when the power is not approximately zero, this indicates that the original scaling should be adjusted to include some dependence on AR.

One example of this is the normalized global radial velocity. The power $\delta=0.4789$ at $Re_g=110$ and 0.7673 at $Re_c=63.5$, which are both more than 100% larger in magnitude compared to the powers χ for the advection or ψ for the PVTr, indicating that the radial velocity scale should be adjusted accordingly. This is similarly true for the radial vorticity where there is clearly a non-linear dependence on AR not currently accounted for. Finally, the tangential and vertical velocity scales should likewise be adjusted although to a lesser degree. Additionally, the powers given in Table B3 show some dependence on Re. Upon comparing the powers between the

 $Re_g = 110$ and $Re_c = 63.5$ cases (which are actually Re_g increasing with AR due to the increasing tip velocity, Fig. 2), it is apparent that the majority of these powers change in magnitude by more than 60%. However, the change in the leading coefficients always remains below roughly 30%. Despite this, combining the two length scales appropriately, along with the predicted velocity and vorticity scales, still accurately predicts the global behavior of the vorticity advection and PVTr.

Moreover, there are non-linear effects that should be addressed; these are most clearly seen in the radial velocity and PVTr. Recall for the predicted scaling of the PVTr, $2\Omega^2 Ro^{\psi+1} \approx 2\Omega^2 Ro$ since the power $\psi \approx 0$. This scaling term for the PVTr is derived with the original velocity scale.35 However, as has just been established, the radial velocity scale should be adjusted to be U_gRo^{δ} based on Eq. (8d). Using this adjusted velocity scale in place of the previous velocity scale results in $2\Omega^2 Ro^{\delta+1}$, where the power δ is different by upwards of 300% compared to the power ψ as measured for the PVTr. The reason for this difference is due to how the global averages were calculated. Specifically, when calculating the global average of the PVTr, the global average of the vertical gradient of radial velocity was considered, i.e., $(\partial u_r/\partial y)$. However, when including the radial velocity scale, it is the vertical gradient of the global average of radial velocity that was considered, i.e., $\partial \tilde{u}_r / \partial y$. This implies that the non-linear effects in the local radial velocity [particularly near the tip likely due to higher tip velocities at $Re_c = 63.5$, Fig. 15(a)] are not removed when using the component based adjusted scale for the global average. This is despite taking advantage of geometricsimilarity to remove some 3D effects near the tip, which was partially successful for the global advection and PVTr.

There is also evidence that the anisotropy is not exclusive to the length scales but may also apply to other scaling terms for the vorticity dynamics. This suggests that seeking a single scaling term may be inappropriate; instead, the scale may depend on the spatial direction being considered. Specifically, a scaling term can be derived for each of the two gradients in the radial vorticity, i.e., $\omega_r = \partial u_y / \partial t - \partial u_t / \partial y$. Using the length scales and updated velocity scales, the



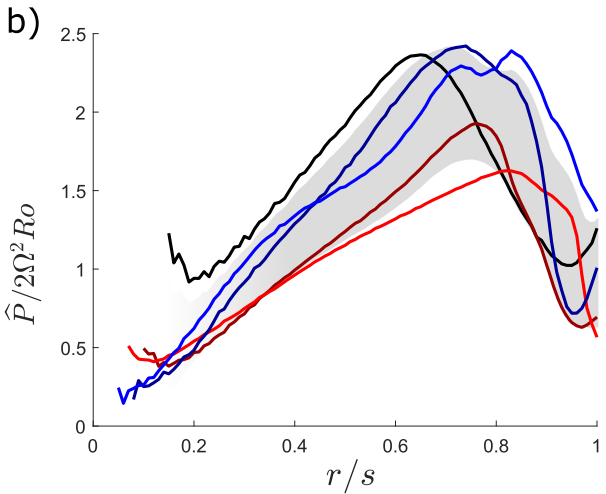


FIG. 15. Spatial-averaged normalized local (a) radial velocity $\widehat{u_r}/U_g$ and (b) PVTr $\widehat{P}/2\Omega^2Ro$ plotted against the local radial position normalized by the span r/s. The black curve represents the baseline case AR=3, $Re_g=110$, while the red curves represent constant U_{tip} and the blue curves represent constant Ω following Fig. 2. The gray regions represent one standard deviation above and below the mean.

first gradient should be proportional to ΩRo^{γ} , while the second gradient is expected to scale with $\Omega Ro^{\beta+1}$. Neither of the powers in these terms agree well with the measured scaling for the radial vorticity ΩRo^{α} , although $\beta+1$ is closer than γ . However, if a single vorticity scaling term is required, then the appropriate choice may depend on which of the two gradients is more dominant similar to the scaling derived by Blasius for the 2D boundary layer. ¹⁶ Additionally, any non-linear effects should be considered as well.

Finally, it is important to note that the global applicability of any scaling term does not necessarily carry over to the local trends. For example, the trends observed in the local PVTr [Fig. 15(b)] after being normalized by $2\Omega^2Ro$ do not all collapse onto each other. When $Re_g=110$ where the tip velocity remains constant across AR, the slopes of the curves decrease with increasing AR, whereas when

 $Re_c = 63.5$ and the angular velocity is constant, the slopes are similar. A comparable observation is seen for the trends in local radial vorticity [Fig. B9(d)], and all of the normalized local trends are provided in supplementary material B. This is likely due to some combination of the effects mentioned previously and should be considered when developing future normalizations of the vorticity within the LEV.

IV. CONCLUSIONS

The primary focus of this study was to identify the correct global scaling for the vorticity advection and PVTr with AR. Different definitions of the Reynolds number also allowed us to separately examine the effects of the tip velocity and angular velocity on the vorticity advection, PVTr, and three-dimensional effects independently.

We first time-averaged the flow within the LEV control-volume and then normalized the vorticity advection and PVTr global averages using both the span and the chord separately. From there, we identified that the span was better suited for normalizing the vorticity advection, whereas the chord was better for the PVTr, i.e., using the span to normalize the vorticity advection and the chord for the PVTr resulted in both terms being roughly constant with increasing AR. Therefore, at least two length scales need to be applied to correctly normalize the vorticity dynamics for revolving wings at these AR and Re. We verified that the tangential and radial directions scale with the span, while the vertical direction should scale with a shorter orthogonal length scale based on the geometry of the LEV crosssectional area and vertical depth, namely, the chord. The tangential length scale was confirmed by applying different length scale combinations when normalizing the local cross-sectional LEV area, where it was found that normalizing the area by the product of the radius of gyration and the chord collapsed all of the curves onto each other outside of the tip region.

It was observed that simply applying the span and chord separately as individual length scales was not enough to normalize the vorticity advection global average due to the three contributions to the vorticity advection requiring different length scales. Additionally, because the flow profiles near the tip region are geometrically dissimilar to those within a range roughly corresponding to 40%–80% of the wing-span in nearly all cases, portions of the LEV control-volume were removed calculating the global averages. The exact size and location of these regions were determined by fitting power laws and removing pieces of the control-volume from the root, tip, or both until the coefficient of determination was optimized for each flow variable. Once the geometrically dissimilar regions were removed, and the separate length scales and power laws were applied to each term, several trends were observed in the different contributions to the vorticity advection.

Using the power law scaling equations for each of the flow variables, we were able to predict the scaling behavior and relative strength of the different contributions to the vorticity advection with increasing AR ($3 \le AR \le 7$) covering the majority of the range found in natural fliers. The tangential advection was shown to be the strongest of the three contributions, followed by the vertical and radial. The tangential advection was roughly independent of AR, while the vertical and radial advections are expected to increase with AR at constant Re_g . However, due to the tangential advection being dominant, it is expected that at larger AR, the flows will be

more comparable with translating wings⁸ where the flow is primarily shed into the wake and not recirculated above the wing forming the LEV. Furthermore, the relative magnitudes of each vorticity advection term are in good agreement with those reported in the previous literature.²⁷⁻³¹ However, we do understand that this set of AR is limited, since it only includes three values. Therefore, we plan on developing a more comprehensive scaling analysis using more AR values (using different chord lengths) covering a similar range in the future, including other terms from the relative vorticity equation.

Finally, it was observed that the normalization used was not consistently able to remove the combined effects of AR and Re_g on all of the flow variables locally. All the normalized local velocity and the vorticity advection curves collapsed onto each other within one standard deviation from the mean. However, both the normalized local radial vorticity and PVTr curves did not collapse onto each other, indicating that the normalization for these terms should be revisited. The same trend that was observed in the dimensional radial vorticity was still apparent after normalization. The slopes of the normalized curves decreased when the tip velocity was held constant as expected, but the slopes increased with AR when the angular velocity was constant despite the local wing velocities being the same at the shared radial positions. On the other hand, although the slopes of the normalized curves of the PVTr were in good agreement when the angular velocity was constant, but when the tip velocity was held constant, the slopes continued to decrease.

Although we have successfully determined the proper length scales involved in flows over rotating wings at these AR and Re_g by testing the normalization of the global vorticity advection and PVTr, more work needs to be done to understand the vorticity dynamics involved since the current normalization failed to eliminate the AR and Re_{σ} effects on the local radial vorticity and PVTr. Further experiments or simulations should be performed to thoroughly investigate the vorticity dynamics involved in the PVTr and vorticity advection at different AoA to develop a more comprehensive and refined set of scaling laws involving all of the relevant parameters. Finally, it remains unclear exactly what role the PVTr plays in LEV stability. It is clear that the PVTr works to remove radial vorticity, but whether this contributes to LEV stability and attachment still needs to be confirmed. Therefore, we also intend to perform additional experiments that will directly identify this role by perturbing the PVTr.

SUPPLEMENTARY MATERIAL

For additional information, see supplementary material A regarding the identification of the quasi-steady period and supplementary material B regarding the geometric-similarity, global averaging, nonlinear regressions and the statistical analysis.

ACKNOWLEDGMENTS

The authors would like to thank all those who made this research possible: Aaron J. Siver, Nicholas Potts, and Autumn J. Werner who aided in the preparation of this manuscript with their careful reviews and Skipper Kagamaster and Ryan Whitacre who provided useful discussion on the statistical analysis.

This research was supported by the National Science Foundation (Grant Nos. CBET-1903312, CMMI-1554429, and CPS-1931929) and the Office of Naval Research-Multidisciplinary University Research Initiatives (Grant No. N00014-14-1-0533).

DATA AVAILABILITY

The data that support the findings of this study are available from the corresponding author upon reasonable request.

REFERENCES

- ¹T. Maxworthy, "Experiments on the Weis-Fogh mechanism of lift generation by insects in hovering flight. Part 1. Dynamics of the 'fling,'" J. Fluid Mech. 93, 47-63
- ²C. P. Ellington, C. Van Den Berg, A. P. Willmott, and A. L. R. Thomas, "Leadingedge vortices in insect flight," Nature 384, 626-630 (1996).
- ³J. R. Usherwood and C. P. Ellington, "The aerodynamics of revolving wings I. Model hawkmoth wings," J. Exp. Biol. 205, 1547-1564 (2002), available at https://jeb.biologists.org/content/205/11/1547.short.
- ⁴D. R. Warrick, B. W. Tobalske, and D. R. Powers, "Aerodynamics of the hovering hummingbird," Nature 435, 1094-1097 (2005).
- ⁵F. T. Muijres, L. C. Johansson, R. Barfield, M. Wolf, G. R. Spedding, and A. Hedenström, "Leading-edge vortex improves lift in slow-flying bats," Science 319, 1250-1253 (2008).
- ⁶M. H. Dickinson, F.-O. Lehmann, and S. P. Sane, "Wing rotation and the aerodynamic basis of insect flight," Science 284, 1954-1960 (1999).
- ⁷J. M. Birch, W. B. Dickson, and M. H. Dickinson, "Force production and flow structure of the leading edge vortex on flapping wings at high and low Reynolds numbers," J. Exp. Biol. 207, 1063-1072 (2004).
- ⁸D. Lentink and M. H. Dickinson, "Rotational accelerations stabilize leading edge vortices on revolving fly wings," J. Exp. Biol. 212, 2705-2719 (2009).
- ⁹D. Lentink and M. H. Dickinson, "Biofluiddynamic scaling of flapping, spinning and translating fins and wings," J. Exp. Biol. 212, 2691-2704
- 10 A. R. Jones and H. Babinsky, "Unsteady lift generation on rotating wings at low Reynolds numbers," J. Aircr. 47, 1013-1021 (2010).
- 11 J. D. Eldredge and A. R. Jones, "Leading-edge vortices: Mechanics and modeling," Annu. Rev. Fluid Mech. 51, 75-104 (2018).
- ¹²S. P. Sane, "The aerodynamics of insect flight," J. Exp. Biol. 206, 4191–4208
- ¹³D. D. Chin and D. Lentink, "Flapping wing aerodynamics: From insects to vertebrates," J. Exp. Biol. 219, 920-932 (2016).
- ¹⁴J. G. Leishman, Journal of the American Helicopter Society, 2nd ed. (Cambridge University Press, New York, 2006), pp. 1-5.
- ¹⁵N. Phillips, K. Knowles, and R. J. Bomphrey, "The effect of aspect ratio on the leading-edge vortex over an insect-like flapping wing," Bioinspiration Biomimetics 10, 056020 (2015).
- ¹⁶P. K. Kundu and I. M. Cohen, Fluid Mechanics (Elsevier, 2010).
- ¹⁷J. Pedlosky, Geophysical Fluid Dynamics (Springer Science & Business Media,
- ¹⁸T. Jardin and L. David, "Spanwise gradients in flow speed help stabilize leadingedge vortices on revolving wings," Phys. Rev. E 90, 013011 (2014).
- ¹⁹T. Jardin and L. David, "Coriolis effects enhance lift on revolving wings," Phys. Rev. E 91, 031001 (2015).
- ²⁰T. Jardin, "Coriolis effect and the attachment of the leading edge vortex," J. Fluid Mech. 820, 312-340 (2017).
- $^{\mathbf{21}}$ T. Jardin and T. Colonius, "On the lift-optimal aspect ratio of a revolving wing at low Reynolds number," J. R. Soc., Interface 15, 20170933 (2018).
- ²²D. Tudball Smith, D. Rockwell, J. Sheridan, and M. C. Thompson, "Effect of radius of gyration on a wing rotating at low Reynolds number: A computational study," Phys. Rev. Fluids 2, 064701 (2017).

- ²³J. D. Anderson, Jr., Fundamentals of Aerodynamics (McGraw-Hill, 1991).
- $^{\mathbf{24}}$ N. Phillips and K. Knowles, "Formation of the leading-edge vortex and spanwise flow on an insect-like flapping-wing throughout a flapping half cycle," Aeronaut. J. 117, 471 (2013), available at https://dspace.lib.cranfield.ac.uk/handle/1826/8104.
- 25 J. M. Birch and M. H. Dickinson, "Spanwise flow and the attachment of the leading-edge vortex on insect wings," Nature 412, 729-733 (2001).
- ²⁶G. V. Lauder, "Aerodynamics: Flight of the robofly," Nature 412, 688-689 (2001)
- ²⁷B. Cheng, S. P. Sane, G. Barbera, D. R. Troolin, T. Strand, and X. Deng, "Threedimensional flow visualization and vorticity dynamics in revolving wings," Exp. Fluids 54, 1423 (2013).
- ²⁸C. J. Wojcik and J. H. J. Buchholz, "Vorticity transport in the leading-edge vortex on a rotating blade," J. Fluid Mech. 743, 249-261 (2014).
- $^{\mathbf{29}}$ W. Shyy and H. Liu, "Flapping wings and aerodynamic lift: The role of leadingedge vortices," AIAA J. 45, 2817-2819 (2007).
- 30 H. Aono, F. Liang, and H. Liu, "Near- and far-field aerodynamics in insect hovering flight: An integrated computational study," J. Exp. Biol. 211, 239-257
- ³¹L. Chen, J. Wu, and B. Cheng, "Volumetric measurement and vorticity dynamics of leading-edge vortex formation on a revolving wing," Exp. Fluids 60, 12
- ³²J. S. Han, J. W. Chang, and H. K. Cho, "Vortices behavior depending on the aspect ratio of an insect-like flapping wing in hover," Exp. Fluids 56, 181
- 33 T. Jardin, A. Farcy, and L. David, "Three-dimensional effects in hovering flapping flight," J. Fluid Mech. 702, 102-125 (2012).
- 34 A. C. DeVoria and K. Mohseni, "On the mechanism of high-incidence lift generation for steadily translating low-aspect-ratio wings," J. Fluid Mech. 813, 110-126
- 35 N. H. Werner, H. Chung, J. Wang, G. Liu, J. M. Cimbala, H. Dong, and B. Cheng, "Radial planetary vorticity tilting in the leading-edge vortex of revolving wings," Phys. Fluids 31, 041902 (2019).
- ³⁶R. R. Harbig, J. Sheridan, and M. C. Thompson, "Reynolds number and aspect ratio effects on the leading-edge vortex for rotating insect wing planforms," J. Fluid Mech. 717, 166-192 (2013).
- ${\bf ^{37}}{\rm H.}$ Dumitrescu and V. Cardoş, "Rotational effects on the boundary-layer flow in wind turbines," AIAA J. 43, 2268-2269 (2003).
- ³⁸H. Dumitrescu and V. Cardoş, "Inboard stall delay due to rotation," J. Aircr. **49**, 101-107 (2012).
- $^{\bf 39}{\rm C.~P.}$ Ellington, "The aerodynamics of hovering insect flight. II. Morphological parameters," Philos. Trans. R. Soc., B 305, 17-40 (1984).
- ⁴⁰W. Shyy, H. Aono, C.-k. Kang, and H. Liu, An Introduction to Flapping Wing Aerodynamics (Cambridge University Press, 2013).
- ⁴¹Y. J. Lee, K. B. Lua, and T. T. Lim, "Aspect ratio effects on revolving wings with Rossby number consideration," Bioinspiration Biomimetics 11, 056013
- ⁴²R. Mittal, H. Dong, M. Bozkurttas, F. M. Najjar, A. Vargas, and A. von Loebbecke, "A versatile sharp interface immersed boundary method for incompressible flows with complex boundaries," J. Comput. Phys. 227, 4825-4852 (2008).
- ⁴³C. Li, H. Dong, and B. Cheng, "Effects of aspect ratio and angle of attack on tip vortex structures and aerodynamic performance for rotating flat plates," in 47th AIAA Fluid Dynamics Conference, June 2017 (AIAA, 2017), pp. 1-16.

- ⁴⁴C. Li, H. Dong, and B. Cheng, "Tip vortices formation and evolution of rotating wings at low Reynolds numbers," Phys. Fluids **32**, 021905 (2020).
- ⁴⁵G. Liu, H. Dong, and C. Li, "Vortex dynamics and new lift enhancement mechanism of wing-body interaction in insect forward flight," J. Fluid Mech. 795, 634-651 (2016).
- ⁴⁶C. Li and H. Dong, "Wing kinematics measurement and aerodynamics of a dragonfly in turning flight," Bioinspiration Biomimetics 12, 026001 (2017).
- ⁴⁷Y. Ren, H. Dong, X. Deng, and B. W. Tobalske, "Turning on a dime: Asymmetric vortex formation in hummingbird maneuvering flight," Phys. Rev. Fluids 1, 050511 (2016).
- ⁴⁸J. Wang, Y. Ren, C. Li, and H. Dong, "Computational investigation of wingbody interaction and its lift enhancement effect in humming bird forward flight." Bioinspiration Biomimetics 14, 046010 (2019).
- ⁴⁹G. Liu, Y. Ren, H. Dong, O. Akanyeti, J. C. Liao, and G. V. Lauder, "Computational analysis of vortex dynamics and performance enhancement due to bodyfin and fin-fin interactions in fish-like locomotion," J. Fluid Mech. 829, 65-88
- ⁵⁰ J. Wang, D. K. Wainwright, R. E. Lindengren, G. V. Lauder, and H. Dong, "Tuna locomotion: A computational hydrodynamic analysis of finlet function," J. R. Soc., Interface 17, 20190590 (2020).
- ⁵¹H. Dong, Z. Liang, and M. Harff, "Optimal settings of aerodynamic performance parameters in hovering flight," Int. J. Micro Air Veh. 1, 173-181
- ⁵² J. Wang, J. Xi, P. Han, N. Wongwiset, J. Pontius, and H. Dong, "Computational analysis of a flapping uvula on aerodynamics and pharyngeal wall collapsibility in sleep apnea," J. Biomech. 94, 88-98 (2019).
- 53 H. Dong, R. Mittal, and F. M. Najjar, "Wake topology and hydrodynamic performance of low-aspect-ratio flapping foils," J. Fluid Mech. 566, 309-343
- ⁵⁴R. Noda, T. Nakata, and H. Liu, "Effects of wing deformation on aerodynamic performance of a revolving insect wing," Acta Mech. Sin. 30, 819-827 (2014).
- 55 J. Wu, L. Chen, C. Zhou, S.-J. Hsu, and B. Cheng, "Aerodynamics of a flapping-
- perturbed revolving wing," AIAA J. 57, 1–16 (2018). ⁵⁶G. Luo and M. Sun, "The effects of corrugation and wing planform on the aerodynamic force production of sweeping model insect wings," Acta Mech. Sin. 21, 531-541 (2005).
- ⁵⁷ A. R. Jones, A. Medina, H. Spooner, and K. Mulleners, "Characterizing a burst leading-edge vortex on a rotating flat plate wing," Exp. Fluids 57, 52 (2016).
- ⁵⁸J. Jeong and F. Hussain, "On the identification of a vortex," J. Fluid Mech. 285, 69-94 (1995).
- ⁵⁹F. M. Bos, B. W. van Oudheusden, and H. Bijl, "Wing performance and 3-D vortical structure formation in flapping flight," J. Fluids Struct. 42, 130-151
- ⁶⁰S. V. Patankar, in *Numerical Heat Transfer and Fluid Flow*, edited by W. J. Minkowycz and E. M. Sparrow (Taylor & Francis, 1980).
- ⁶¹ W. H. Hager, "Blasius: A life in research and education," Exp. Fluids 34, 566-571
- 62 I. Woiwood, D. R. Reynolds, and C. D. Thomas, "Insect movement: Mechanisms and consequences," in Proceedings of the Royal Entomological Society's 20th Symposium, London, UK, September 1999, 2001.
- ⁶³Z. R. Carr, A. C. Devoria, and M. J. Ringuette, "Aspect-ratio effects on rotating wings: Circulation and forces," J. Fluid Mech. 767, 497-525 (2015).